5. R. O. Pepin, *Icarus* **92**, 2 (1991).
6. R. O. Pepin, *Earth Planet. Sci. Lett.* **252**, 1 (2006).
7. S. Sasaki, *Icarus* **91**, 29 (1991).
8. T. Owen, A. Bar-Nun, I. Kleinfeld, *Nature* **358**, 43 (1992).
9. M. Trieloff, J. Kunz, C. J. Allegre, *Earth Planet. Sci. Lett.* **200**, 297 (2002).
10. C. J. Ballentine, B. Marty, B. Sherwood Lollar, M. Cassidy, *Nature* **433**, 33 (2005).
11. B. Marty *et al.*, *Science* **319**, 75 (2008).
12. G. Notesco, D. Laufer, A. Bar-Nun, T. Owen, *Icarus* **142**, 298 (1999).
13. A. Morbidelli *et al.*, *Meteorit. Planet. Sci.* **35**, 1309 (2000).
14. C. Allègre, T. Staudacher, P. Sarda, *Earth Planet. Sci. Lett.* **81**, 127 (1987).
15. C. L. Harper Jr., S. B. Jacobsen, *Science* **273**, 1814 (1996).
16. G. Holland, C. J. Ballentine, *Nature* **441**, 186 (2006).
17. C. J. Ballentine, G. Holland, *Philos. Trans. R. Soc. London Ser. A* **366**, 4183 (2008).
18. T. Staudacher, *Nature* **325**, 605 (1987).
19. M. W. Caffee *et al.*, *Science* **285**, 2115 (1999).
20. Materials and methods are available as supporting material on *Science* Online.
21. R. O. Pepin, D. Porcelli, *Earth Planet. Sci. Lett.* **250**, 470 (2006).
22. M. Moreira, J. Kunz, C. Allègre, *Science* **279**, 1178 (1998).
23. D. Porcelli, G. J. Wasserburg, *Geochim. Cosmochim. Acta* **59**, 4921 (1995).
24. P. Signer, H. E. Suess, *Earth Science and Meteoritics*, J. Geiss, E. D. Goldberg, Eds. (North-Holland, Amsterdam, 1963).
25. T. M. Donahue, *Icarus* **66**, 195 (1986).
26. M. Touboul, T. Kleine, B. Bourdon, H. Palme, R. Wieler, *Nature* **450**, 1206 (2007).
27. T. J. Ahrens, *Annu. Rev. Earth Planet. Sci.* **21**, 525 (1993).
28. H. Genda, Y. Abe, *Nature* **433**, 842 (2005).
29. A. Bar-Nun, I. Kleinfeld, E. Kochavi, *Phys. Rev. B* **38**, 7749 (1988).
30. N. Dauphas, *Icarus* **165**, 326 (2003).
31. R. O. Pepin, *Space Sci. Rev.* **106**, 211 (2003).
32. D. York, *Earth Planet. Sci. Lett.* **5**, 320 (1969).

33. We thank Oxy and Amerada Hess corporations for permission to sample the Bravo Dome Field. We thank D. Blagburn and B. Clementson for laboratory support and R. Pepin for discussions on the manuscript. This work was funded by UK Natural Environment Research Council.

Supporting Online Material

www.sciencemag.org/cgi/content/full/326/5959/1522/DC1
Materials and Methods
Figs. S1 to S5
Tables S1 to S4
References

22 July 2009; accepted 23 October 2009
10.1126/science.1179518

Evolution of Organic Aerosols in the Atmosphere

J. L. Jimenez,[1]* M. R. Canagaratna,[2] N. M. Donahue,[3] A. S. H. Prevot,[4]* Q. Zhang,[5,6] J. H. Kroll,[2,7] P. F. DeCarlo,[1,4,8] J. D. Allan,[9,10] H. Coe,[9] N. L. Ng,[2] A. C. Aiken,[1]† K. S. Docherty,[1] I. M. Ulbrich,[1] A. P. Grieshop,[3]‡ A. L. Robinson,[3] J. Duplissy,[4]§ J. D. Smith,[11] K. R. Wilson,[11] V. A. Lanz,[4,12] C. Hueglin,[12] Y. L. Sun,[5,6] J. Tian,[5] A. Laaksonen,[13,14] T. Raatikainen,[13,14] J. Rautiainen,[13] P. Vaattovaara,[13] M. Ehn,[15] M. Kulmala,[15,16] J. M. Tomlinson,[17]‖ D. R. Collins,[17] M. J. Cubison,[1] E. J. Dunlea,[1]¶ J. A. Huffman,[1]# T. B. Onasch,[2] M. R. Alfarra,[4,9,10] P. I. Williams,[9,10] K. Bower,[9] Y. Kondo,[18] J. Schneider,[19] F. Drewnick,[5,19] S. Borrmann,[19,20] S. Weimer,[4,5,21] K. Demerjian,[5] D. Salcedo,[22] L. Cottrell,[23]†† R. Griffin,[23,24] A. Takami,[25] T. Miyoshi,[25]‡‡ S. Hatakeyama,[25]§§ A. Shimono,[26] J. Y Sun,[27] Y. M. Zhang,[27] K. Dzepina,[1,28]¶¶ J. R. Kimmel,[1,2,29] D. Sueper,[1,2] J. T. Jayne,[2] S. C. Herndon,[2]‖‖ A. M. Trimborn,[2] L. R. Williams,[2] E. C. Wood,[2] A. M. Middlebrook,[30] C. E. Kolb,[2] U. Baltensperger,[4] D. R. Worsnop[2,13,14,15]

Organic aerosol (OA) particles affect climate forcing and human health, but their sources and evolution remain poorly characterized. We present a unifying model framework describing the atmospheric evolution of OA that is constrained by high–time-resolution measurements of its composition, volatility, and oxidation state. OA and OA precursor gases evolve by becoming increasingly oxidized, less volatile, and more hygroscopic, leading to the formation of oxygenated organic aerosol (OOA), with concentrations comparable to those of sulfate aerosol throughout the Northern Hemisphere. Our model framework captures the dynamic aging behavior observed in both the atmosphere and laboratory: It can serve as a basis for improving parameterizations in regional and global models.

Submicron atmospheric aerosols exert a highly uncertain effect on radiative climate forcing (*1*) and have serious impacts on human health (*2*). Organic aerosol (OA) makes up a large fraction (20 to 90%) of the submicron particulate mass (*3*, *4*). However, OA sources, atmospheric processing, and removal are very uncertain. Primary OA (POA) is directly emitted from fossil fuel combustion, biomass burning, and other sources, but the atmospheric evolution of POA after emission remains poorly characterized (*3*, *4*). Recent results show that secondary OA (SOA), formed by atmospheric oxidation of gas-phase species, accounts for a large fraction of the OA burden (*3*, *5*–*9*). Despite much recent progress in our understanding of SOA formation chemistry (*10*), current "bottom-up" models based on parameterizations of laboratory experiments cannot explain the magnitude and evolution of atmospheric SOA (*5*–*9*). Explicit chemical models are still not able to predict ambient SOA concentrations or degree of oxidation accurately, and they are too complex for large-scale models (*11*). A better understanding of the chemical evolution of OA is required to reduce unacceptable aerosol-related uncertainties in global climate simulations (*12*) and to improve air quality (*13*).

Here we integrate observations and modeling to better characterize the physical and chemical properties and climate effects of OA. Field and laboratory data show that the volatility and oxidation state of organics can be used to build a two-dimensional (2D) modeling framework that maps the evolution of atmospheric OA. The measurements and model reveal OA to be a highly dynamic system, tightly coupled to gas-phase oxidation chemistry. Gas-phase reactions transform OA constituents, and the OA itself is an intermediate, often forming from gas-phase precursors and ultimately returning, in part, to gas-phase products. The framework, though computationally inexpensive, allows an accurate representation of OA in regional and global climate and air-quality models used for policy assessments.

The aerosol mass spectrometer (AMS) detects OA quantitatively by combining thermal vaporization and electron ionization (EI) (*14*). Factor analysis of AMS data (FA-AMS) (*3*, *15*–*17*) demonstrates that AMS data contain sufficient information to differentiate several types of OA and to determine their dry oxygen content (*18*). FA-AMS is based on the total OA mass and avoids the challenges of techniques based on molecular tracers with highly variable tracer:OA ratios (*19*) that may not be stable against atmospheric oxidation (*20*). Figure 1 summarizes FA-AMS results at many locations in the Northern Hemisphere, with typical high-resolution component spectra shown in fig. S1 (*21*). POA from fossil fuel combustion and other urban sources [hydrocarbon-like OA (HOA)] and biomass-burning OA (BBOA) have been identified in multiple studies. However, most OA mass at many locations is oxygenated organic aerosol (OOA) (*3*), characterized by its high oxygen content, with an atomic O:C ratio (an indicator of oxidation state) of 0.25 to ~1 for highly aged OA (*18*). There is strong evidence that most atmospheric OOA is secondary: Increases in OOA are strongly correlated with photochemical activity (*7*, *22*) and other secondary species (*7*, *16*, *17*, *22*), and OOA levels are consistent with SOA estimates using other methods (*13*, *15*).

At many locations, FA-AMS identifies two subtypes of OOA that differ in volatility and O:C (Fig. 1). Volatility and O:C are generally inversely correlated (*16*–*18*, *23*, *24*). Low-volatility OOA (LV-OOA, empirical formula ~$C_8O_{5.5}H_{10}$) is strongly correlated with nonvolatile secondary species such as sulfate and has a high O:C (Fig. 1, inset), consistent with regional, heavily aged OA. Semi-volatile OOA (SV-OOA, empirical formula ~$C_8O_3H_{11}$) has a higher correlation with semivolatile species such as ammonium nitrate and ammonium chloride and has a lower O:C, consistent with less–photochemically aged OA. These two OOA subtypes offer a lumped description of SOA components based on their distinct physicochemical properties. The relative concentrations of the OOA subtypes depend on both ambient temperature and photochemistry. For the three sites with both win-

ter and summer measurements, for example, SV-OOA was observed only during the summer, when the dynamic range in ambient temperature and photochemical conditions is larger.

Recent field and laboratory experiments illustrate the fact that atmospheric oxidation reactions result in the dynamic evolution of OA properties with age. This evolution contrasts sharply with the relatively static nature of sulfate aerosol. In general, atmospheric SV-OOA corresponds to fresh SOA that evolves into LV-OOA with additional photochemical processing. Figure 2, A and B, present data acquired around Mexico City aboard the National Center for Atmospheric Research/National Science Foundation C-130 aircraft during the Megacity Initiative: Local and Global Research Observations (MILAGRO) campaign (*25*). This megacity experiences substantial particulate pollution, including intense SOA formation (*7*, *18*, *22*, *23*, *25*). The aircraft flew over a ground supersite located inside the city (designated as T0) and two sites 30 and 63 km downwind (designated T1 and T2) in the afternoon, corresponding to approximate transport times of 0, 3, and 6 hours from the urban area. In the urban area (T0), SV-OOA was already dominant, consistent with previous observations (*7*), but the fraction of OOA, O:C, and the relative LV-OOA contribution all increased with aging (T0→T1→T2).

A similar transformation has also been observed in the laboratory (Fig. 2, C to F) for various types of OA (*21*). SOA formed from the oxidation of α-pinene becomes more similar to ambient SV-OOA after some aging and then evolves with continued oxidation to become increasingly similar to ambient LV-OOA (Fig. 2C). SOA formation and heterogeneous oxidation from primary diesel emissions, biomass-burning smoke, and the POA surrogate squalane result in strikingly similar transformations (Fig. 2, D to F). The bulk OA spectra in each experiment initially resemble the appropriate source aerosol spectra, but as photochemistry proceeds, their signature is transformed and the laboratory OA spectra become more similar first to that of ambient SV-OOA and then increasingly to that of LV-OOA. These observations, when taken together, indicate that atmospheric oxidation of OA converges toward highly aged LV-OOA regardless of the original OA source, with the original source signature being replaced by that of atmospheric oxidation. This is consistent with the previously reported ubiquity in atmospheric OA of humic-like substances (HULIS), which are complex mixtures of high–molecular-weight polycarboxylic acids that are similar to fulvic acids in soil organic matter (*26*).

An important property of aerosols is hygroscopicity (propensity to absorb water vapor). A more hygroscopic particle of a given size will grow more under humid conditions, scattering more incident light; it will also be more likely to form cloud droplets. Both phenomena strongly influence the radiative forcing of climate through the direct and indirect effects of aerosols (*1*). The dependence of hygroscopicity on particle composition can be represented with the single parameter κ (*27*). Figure 3 shows the relationship between organic O:C and κ for ambient aerosols in urban, forested, and remote locations and also for SOA formed in laboratory chambers from three different precursors (*21*); O:C and κ were determined by AMS and hygroscopicity tandem differential mobility analyzer (HTDMA) (*28*) measurements, respectively. A trend of increasing hygroscopicity with increasing O:C is robust. This strongly suggests that a model must reproduce the evolution of OA shown in Fig. 2 to estimate the variations in OA hygroscopicity, allowing the effects of OA on global climate to be determined more accurately in atmospheric models.

Traditional SOA models are based on the parameterization of smog-chamber experiments, often using a two-product absorptive partitioning scheme (*10*). These models typically do not capture either the amount of SOA or the substantial aging observed in field experiments described above (*7*). Recently, Robinson *et al*. (*29*) proposed an OA model scheme based on lumping species into volatility bins of a basis set (specified as decades in saturation concentration, C^*, at 298 K). This resulted in improved agreement between regional model predictions and ambient measurements. However, simplified lumping schemes based only on volatility cannot represent the broad diversity in physicochemical properties of organic species, such as polarity, solubility, carbon number, and reactivity, and thus may not reproduce the formation rates, properties, or atmospheric fates of OA.

The discussion above underscores the fact that the oxygen content and volatility of OA evolve with photochemical processing. This motivated development of a 2D volatility basis set (2D-VBS) modeling framework using OA volatility (C^*) and oxidation state (here approximated by oxygen content, O:C) as its two basis vectors. Because these two OA properties can be measured in near–real time, this framework can be constrained and directly verified with experimental data, which is an advantage over a previously proposed basis set based on carbon number and polarity (*30*). Moreover, this framework could be used to estimate OA hygroscopicity and would thus introduce an important simplification in atmospheric models.

As shown in Fig. 4, the 2D-VBS (*21*) lumps species with $C^* <\sim 10^7$ μg m^{-3} into bins that are spaced evenly in C^* and O:C space. Each bin includes many organic compounds, spanning only a narrow range of carbon numbers. All constituents are assumed to form a quasi-ideal solution according to standard partitioning theory (*31*). In the atmosphere, only species with $C^* <\sim 10$ μg m^{-3} typically partition substantially into the aerosol (*8*).

Figure 4 shows the location of the OOA factors in the 2D-VBS. Most ambient OA is a mixture of LV-OOA and SV-OOA, with $0.25 <$ O:C $<$ 1 and low C^*. Most primary emissions lie along or near the x axis (low O:C, various C^*). Photochemical reactions cause material to evolve in the 2D space. A key question is, how do primary gas and particle emissions age to become LV-OOA?

The 2D-VBS simulates photochemical aging using a functionalization kernel and a fragmentation kernel, a branching ratio between these two pathways, and a simple representation of differing homogeneous and heterogeneous oxidation by OH (Fig. 4C) (*21*). In the current implementation, the first generation of oxidation is modeled with explicit chemistry but the later generations of oxidation are phenomenological, with param-

[1]Cooperative Institute for Research in the Environmental Sciences and Department of Chemistry and Biochemistry, University of Colorado, Boulder, CO, USA. [2]Aerodyne Research, Billerica, MA, USA. [3]Center for Atmospheric Particle Studies, Carnegie Mellon University, Pittsburgh, PA, USA. [4]Laboratory of Atmospheric Chemistry, Paul Scherrer Institut, Villigen, Switzerland, [5]Atmospheric Sciences Research Center, State University of New York, Albany, NY, USA. [6]Department of Environmental Toxicology, University of California, Davis, CA, USA. [7]Department of Civil and Environmental Engineering, Massachusetts Institute of Technology, Cambridge, MA, USA. [8]Department of Atmospheric and Oceanic Science, University of Colorado, Boulder, CO, USA. [9]School of Earth, Atmospheric, and Environmental Science, University of Manchester, Oxford Road, Manchester, UK. [10]National Centre for Atmospheric Science, University of Manchester, Oxford Road, Manchester, UK. [11]Chemical Sciences Division, Lawrence Berkeley National Laboratory, Berkeley, CA, USA. [12]Empa, Laboratory for Air Pollution/Environmental Technology, Dübendorf, Switzerland. [13]Department of Physics, University of Kuopio, Kuopio, Finland. [14]Finnish Meteorological Institute, Helsinki, Finland. [15]Department of Physics, University of Helsinki, Helsinki, Finland. [16]Department of Applied Environmental Science, Stockholm University, Stockholm, Sweden. [17]Department of Atmospheric Sciences, Texas A&M University, College Station, TX, USA. [18]Research Center for Advanced Science and Technology, University of Tokyo, Tokyo, Japan. [19]Department of Particle Chemistry, Max Planck Institute for Chemistry, Mainz, Germany. [20]Institute for Atmospheric Physics, Johannes Gutenberg University, Mainz, Germany. [21]Empa, Laboratory for Internal Combustion Engines, Dübendorf, Switzerland. [22]Centro de Investigaciones Quimicas, Universidad Autonoma del Estado de Morelos, Cuernavaca, Mexico. [23]Climate Change Research Center, University of New Hampshire, Durham, NH, USA. [24]Department of Civil and Environmental Engineering, Rice University, Houston, TX, USA. [25]Asian Environmental Research Group, National Institute for Environmental Studies, Tsukuba, Japan. [26]Sanyu Plant Service, Sagamihara, Japan. [27]Key Laboratory for Atmospheric Chemistry, Chinese Academy of Meteorological Sciences, Beijing, China. [28]Atmospheric Chemistry Division, National Center for Atmospheric Research, Boulder, CO, USA. [29]Tofwerk, Thun, Switzerland. [30]Earth Science Research Laboratory, National Oceanic and Atmospheric Administration, Boulder, CO, USA.

*To whom correspondence should be addressed. E-mail: jose.jimenez@colorado.edu (J.L.J.); andre.prevot@psi.ch (A.S.H.P.)

†Present address: Swiss Federal Institute of Technology, Zurich, Switzerland.

‡Present address: Institute for Resources, Environment and Sustainability, University of British Columbia, Vancouver, Canada.

§Present address: CERN, Geneva, Switzerland.

||Present address: Pacific Northwest National Laboratory, Richland, WA, USA.

¶Present address: Climate Program Office, National Oceanic and Atmospheric Administration, Silver Spring, MD, USA.

#Present address: Department of Biogeochemistry, Max Planck Institute for Chemistry, Mainz, Germany.

††Present address: Environ International, Groton, MA, USA.

‡‡Present address: Tokyo Metropolitan Research Institute for Environmental Protection, Tokyo, Japan.

§§Present address: Institute of Symbiotic Science and Technology, Tokyo University of Agriculture and Technology, Tokyo, Japan.

|| ||Present address: Shoreline Science Research, Tokyo, Japan.

¶¶Present address: Department of Particle Chemistry, Max Planck Institute for Chemistry, Mainz, Germany.

eters consistent with our current understanding of atmospheric chemistry. It can be applied to material produced from any precursor.

To test whether the model can reproduce the transformations of atmospheric OA shown in Fig. 2, the simulated formation and aging chemistry of α-pinene SOA (and the attendant vapors) are shown in Fig. 4. The full (vapor and particle) first-generation distribution from the α-pinene + O_3 reaction (derived from chamber data) is shown with blue contours in Fig. 4A, having $1 < C^* < 10^7$ μg m^{-3} and $0.1 < O:C < 0.4$. Lower-volatility products to the upper left of the blue contours condense to form SOA. The reaction of the first-generation particle and vapor distribution with OH is modeled with functionalization reactions that generate products that are roughly within the limits indicated by the red dashed lines in Fig. 4A. The predicted condensed-phase products after 1.5 lifetimes of OH oxidation are shown with purple contours in Fig. 4A and the yellow star in Fig. 4, A and B. The model predicts a tripling of SOA mass by the end of the second generation of oxidation. This increase is also accompanied by an increase in O:C, shown in Fig. 4B, and a drop in average C^* of the aerosol. The predictions in Fig. 4 are consistent with observations of *cis*-pinonic acid, a typical first-generation reaction product, and of its OH oxidation product α,α-dimethyltricarballylic acid (*8*). Moreover, the simulation results reproduce the SV-OOA–to–LV-OOA transformation observed in the laboratory experiments on α-pinene SOA aging (Fig. 2C).

The model predicts very similar outcomes for the aging of other SOA precursors, including the evaporated diesel and biomass-burning smoke shown in Fig. 2, E and F. Most of the aging in these simulations occurs via gas-phase oxidation of semivolatile vapors. OOA formation occurs mainly via condensation of the less volatile products of these aging reactions on accumulation-mode particles, where OOA principally resides (*15*). However, in all of these cases, the majority of the oxidation products in the model are higher-volatility gases. Although the current implementation of the framework considers aging only by reactions with OH, other aging mechanisms, such as oligomerization or the addition of hydrated glyoxal to a semivolatile organic in the condensed phase (*32*), could be incorporated into the framework. These mechanisms represent other means of substantially increasing O:C while reducing C^* by several decades.

OA is dynamic and continually evolves in the atmosphere; this evolution strongly influences the effects of particulate matter on climate and air quality. The complex evolution of OA contrasts with the simpler behavior of sulfate, which is irreversibly oxidized and condensed. Current modeling frameworks for OA are constructed in an analogous way to those for sulfate, with either no aging or one-step oxidation. Here we have presented a unifying framework describing the atmospheric evolution of OA, which is directly connected to worldwide observations and experimentally verifiable and can be used to evaluate and form the basis of practical phenomenological modeling

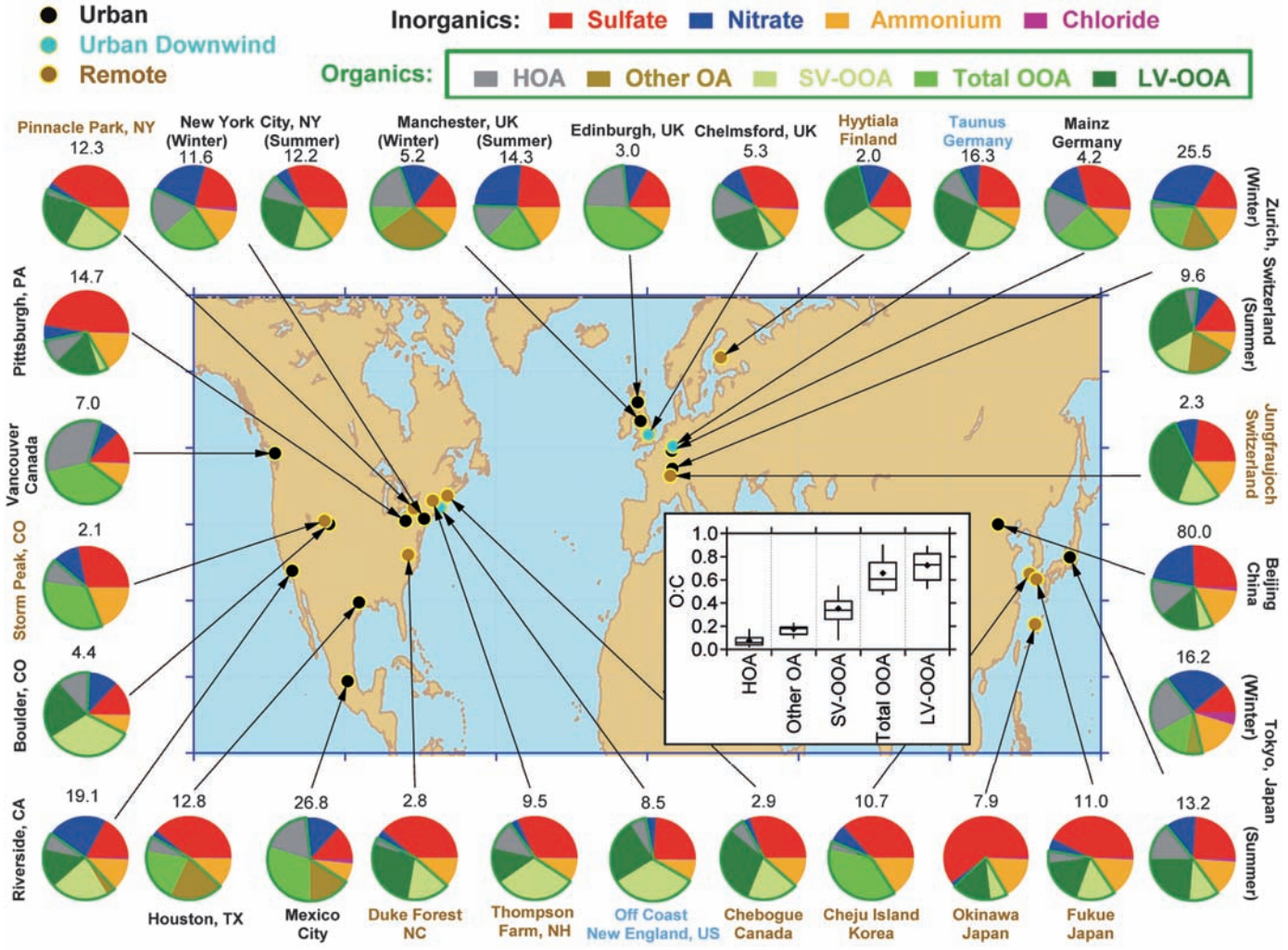

Fig. 1. Total mass concentration (in micrograms per cubic meter) and mass fractions of nonrefractory inorganic species and organic components in submicrometer aerosols measured with the AMS at multiple surface locations in the Northern Hemisphere (*21*). The organic components were obtained with FA-AMS methods (*3*, *15*–*17*). In some studies, the FA-AMS methods identified one OOA factor, whereas in other locations, two types, SV-OOA and LV-OOA, were identified. HOA is a surrogate for urban primary OA, and Other OA includes primary OAs other than HOA that have been identified in several studies, including BBOA. (Inset) Distributions of O:C for the OA components identified at the different sites, calculated according to (*18*).

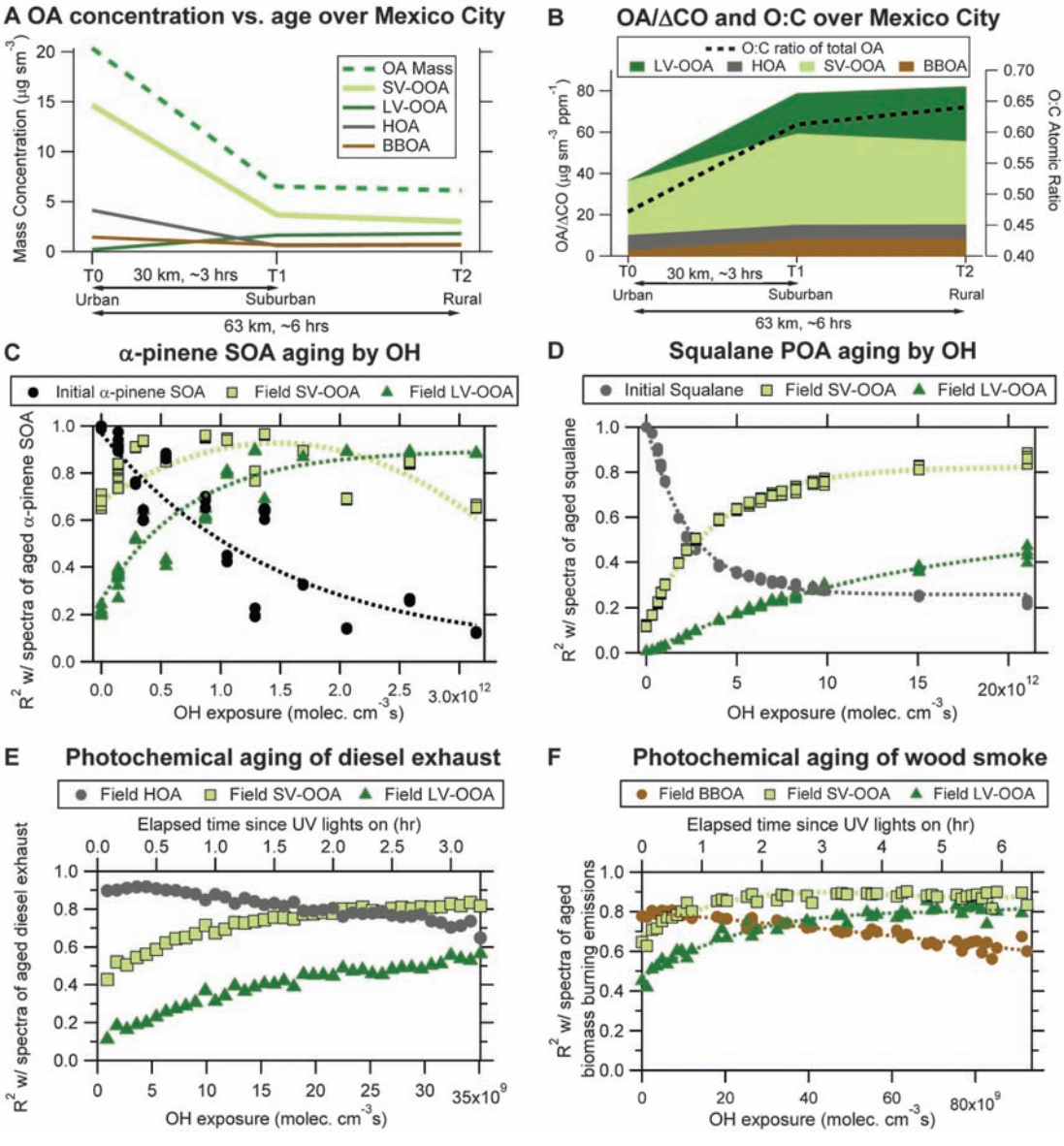

Fig. 2. Field and laboratory data of OA evolution with photochemical aging. (**A** and **B**) Atmospheric aging of OA above the T0→T1→T2 sites in and around Mexico City (corresponding to approximate transport times of 0, 3, and 6 hours from the urban area) as measured from the C-130 aircraft during the MILAGRO field experiment. OA/ΔCO, where ΔCO is the measured CO minus a Northern Hemispheric background of 100 parts per billion by volume, is plotted in (B) to correct for dilution of the air mass. Biomass burning was suppressed by rain during this period. (**C** to **F**) Evolution of OA composition during photochemical aging in laboratory reaction chambers of (C) α-pinene SOA, (D) squalane (a liquid hydrocarbon used as a surrogate for reduced primary OA), (E) diesel exhaust, and (F) biomass-burning smoke. In (C) to (F), the increased degree of oxidation and similarity to ambient OOA spectra are indicated by the Pearson correlation coefficients (R^2) between the evolving total OA spectra in each experiment and the SV-OOA and LV-OOA spectra derived from the Mexico City field data set. The similarity to the initial source spectra decreases in all cases: For α-pinene and squalane, the evolving OA is compared to the original OA, whereas for diesel exhaust and wood smoke, it is compared with ambient HOA and BBOA from Mexico City. Dashed lines are included to guide the eye.

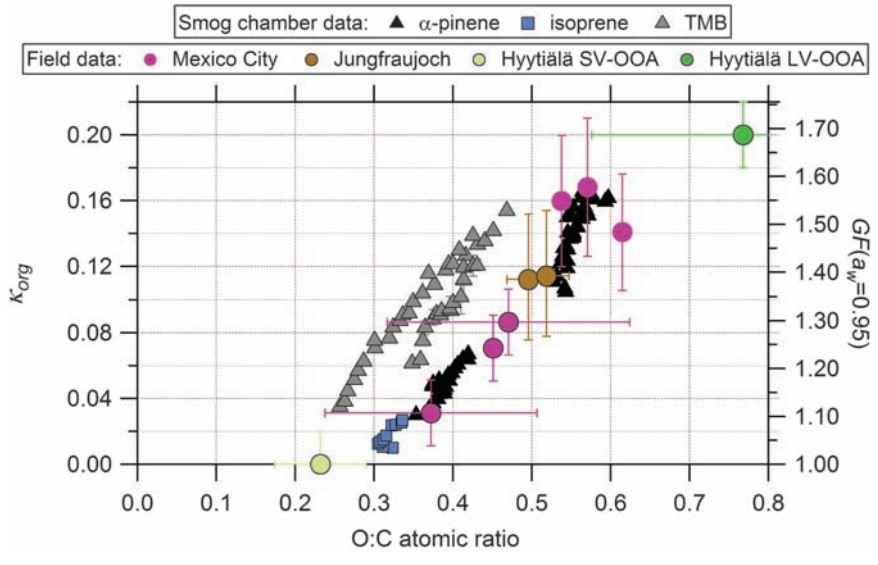

Fig. 3. Relationship between O:C and hygroscopicity (κ, or equivalently the particle growth factor at 95% relative humidity) of OA for several field data sets (a high-altitude site at Jungfraujoch, Switzerland; above Mexico City, a polluted megacity; and at the forested site of Hyytiälä, Finland) and for laboratory smog chamber SOA (*21*). TMB, trimethylbenzene. Error bars represent the uncertainties in O:C and κ_{org} (org, organic) and are shown for only a few data points to reduce visual clutter. *GF*, growth factor; a_w, water activity.

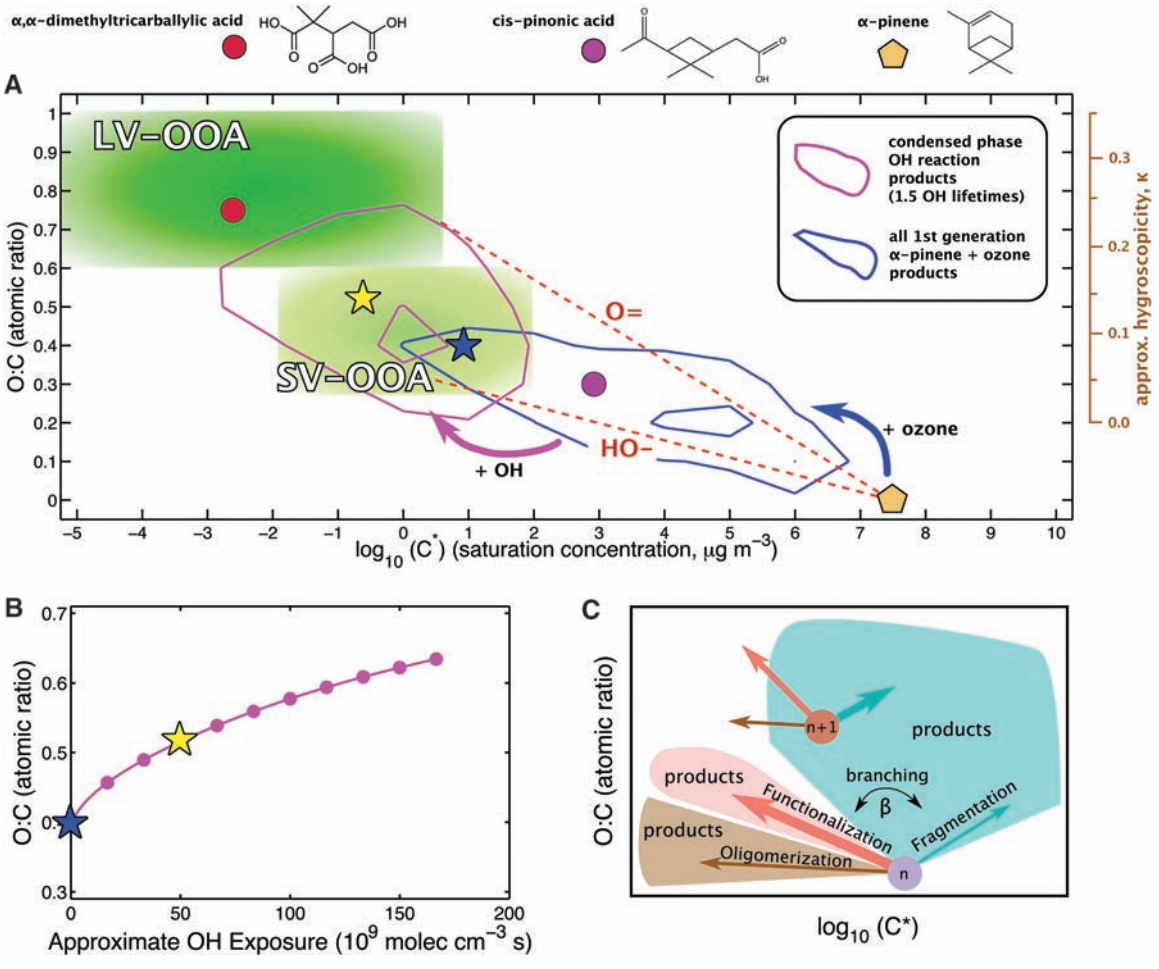

Fig. 4. (**A**) 2D framework for OA aging. The *x* axis is volatility ($\log_{10}$ of C^* at 298 K). The *y* axis is oxidation state, approximated by O:C. The secondary *y* axis shows the approximate κ of α-pinene SOA from Fig. 3. Compounds with $C^* \leq C_{OA}$ (the organic aerosol concentration, typically 1 to 10 μg m^{-3}) favor the condensed phase. Those with $C^* > C_{OA}$ favor the gas phase. The OOA factors described in Figs. 1 to 3 fall in this 2D space as shown by the green areas, with LV-OOA being less volatile and more oxidized than SV-OOA. We modeled the initial oxidation of common precursors with explicit chemistry, but later-generation oxidation applies to material produced from any precursor. α-pinene (brown pentagon) is an example. All products from the α-pinene + ozone reaction, modeled explicitly, are distributed according to the blue contours; the material at low C^* and high O:C forms SOA (with mean properties indicated by the blue star). Typical effects of adding (=O) and (–OH) functionality to a C_{10} backbone are shown with red dashed lines, and a common first-generation product, *cis*-pinonic acid, is shown with a magenta dot. After forming α-pinene SOA explicitly, we modeled subsequent aging reactions with OH within the 2D-VBS. A representative second-generation product, a C_8 triacid, is shown with a crimson dot within the LV-OOA range. Modeled condensed-phase products after 1.5 lifetimes of OH oxidation are shown with purple contours. The mass-weighted average is indicated by the yellow star. This simulation reproduces a substantial shift toward ambient OOA characteristics, indicated by the shift between the blue and yellow stars. (**B**) Evolution of condensed-phase O:C versus approximate OH exposure for simulated aging (similar to Fig. 2C). The blue and yellow stars for organic aerosol in (A) are shown. (**C**) Oxidation can occur in the gas or condensed phase, and reactions transform material as shown (*21*). Reactions form three categories: fragmentation, functionalization, or oligomerization, based on whether the carbon number decreases, stays the same, or increases. Here we model the first two pathways. The branching ratio (β) between these pathways is critical. Functionalization will reduce volatility considerably, whereas fragmentation can generate more-volatile species, which are less likely to partition to the OA.

approaches. The combination of measurements and the modeling framework implies that most OA is an intermediate state of organic material, between primary emissions of reduced species and highly oxidized volatile products (CO and CO_2). Future models, inventories, and measurements will almost certainly need to account for the dynamic sources and sinks of OA to accurately predict regional and global OA distributions and properties and thus the associated health and climate effects.

References and Notes

1. P. Forster *et al.*, in S. Solomon *et al., IPCC 4th Assessment Report* (Cambridge Univ. Press, Cambridge, 2007), chap. 2.
2. A. Nel, *Science* **308**, 804 (2005).
3. Q. Zhang *et al.*, *Geophys. Res. Lett.* **34**, L13801 (2007).
4. D. M. Murphy *et al.*, *J. Geophys. Res.* **111**, D23S32 (2006).
5. C. L. Heald *et al.*, *Geophys. Res. Lett.* **32**, L18809 (2005).
6. J. A. de Gouw *et al.*, *J. Geophys. Res.* **110**, D16305 (2005).
7. R. Volkamer *et al.*, *Geophys. Res. Lett.* **33**, L17811 (2006).
8. M. Hallquist *et al.*, *Atmos. Chem. Phys.* **9**, 5155 (2009).
9. A. H. Goldstein, I. E. Galbally, *Environ. Sci. Technol.* **41**, 1514 (2007).
10. J. H. Kroll, J. H. Seinfeld, *Atmos. Environ.* **42**, 3593 (2008).
11. D. Johnson *et al.*, *Atmos. Chem. Phys.* **6**, 403 (2006).
12. J. T. Kiehl, *Geophys. Res. Lett.* **34**, L22710 (2007).
13. K. S. Docherty *et al.*, *Environ. Sci. Technol.* **42**, 7655 (2008).
14. M. R. Canagaratna *et al.*, *Mass Spectrom. Rev.* **26**, 185 (2007).
15. Q. Zhang, D. R. Worsnop, M. R. Canagaratna, J. L. Jimenez, *Atmos. Chem. Phys.* **5**, 3289 (2005).
16. V. A. Lanz *et al.*, *Atmos. Chem. Phys.* **7**, 1503 (2007).
17. I. M. Ulbrich, M. R. Canagaratna, Q. Zhang, D. R. Worsnop, J. L. Jimenez, *Atmos. Chem. Phys.* **9**, 2891 (2009).
18. A. C. Aiken *et al.*, *Environ. Sci. Technol.* **42**, 4478 (2008).
19. R. Subramanian, N. M. Donahue, A. Bernando-Bricker, W. F. Rogge, A. L. Robinson, *Atmos. Environ.* **40**, 8002 (2006).
20. E. A. Weitkamp, K. E. Huff Hartz, A. M. Sage, N. M. Donahue, A. L. Robinson, *Environ. Sci. Technol.* **42**, 5177 (2008).
21. Materials and methods are available as supporting material on *Science* Online.
22. S. C. Herndon *et al.*, *Geophys. Res. Lett.* **35**, L15804 (2008).
23. J. A. Huffman *et al.*, *Atmos. Chem. Phys.* **9**, 7161 (2009).
24. A. P. Grieshop, N. M. Donahue, A. L. Robinson, *Atmos. Chem. Phys.* **9**, 2227 (2009).
25. P. F. DeCarlo *et al.*, *Atmos. Chem. Phys.* **8**, 4027 (2008).
26. S. Fuzzi *et al.*, *Geophys. Res. Lett.* **28**, 4079 (2001).
27. M. D. Petters, S. M. Kreidenweis, *Atmos. Chem. Phys.* **7**, 1961 (2007).
28. D. J. Rader, P. H. McMurry, *J. Aerosol Sci.* **17**, 771 (1986).
29. A. L. Robinson *et al.*, *Science* **315**, 1259 (2007).
30. J. F. Pankow, K. C. Barsanti, *Atmos. Environ.* **43**, 2829 (2009).
31. J. F. Pankow, *Atmos. Environ.* **28**, 189 (1994).
32. R. Volkamer *et al.*, *Geophys. Res. Lett.* **34**, L19807 (2007).

33. This work was supported by NSF's Atmospheric Chemistry Program, the Environmental Protection Agency's Science to Achieve Results program, the Department of Energy's Office of Biological and Environmental Research/Atmospheric Science Program, the National Oceanic and Atmospheric Administration Office of Global Programs, the Swiss NSF, EUROCHAMP, and other funding agencies listed in table S1.

Supporting Online Material

www.sciencemag.org/cgi/content/full/326/5959/1525/DC1
Materials and Methods
Figs. S1 to S3
Tables S1 to S4
References

10 August 2009; accepted 6 November 2009
10.1126/science.1180353

Supporting Online Material for

Evolution of Organic Aerosols in the Atmosphere

J. L. Jimenez,* M. R. Canagaratna, N. M. Donahue, A. S. H. Prevot,* Q. Zhang, J. H. Kroll, P. F. DeCarlo, J. D. Allan, H. Coe, N. L. Ng, A. C. Aiken, K. D. Docherty, I. M. Ulbrich, A. P. Grieshop, A. L. Robinson, J. Duplissy, J. D. Smith, K. R. Wilson, V. A. Lanz, C. Hueglin, Y. L. Sun, J. Tian, A. Laaksonen, T. Raatikainen, J. Rautiainen,, P. Vaattovaara, M. Ehn, M. Kulmala, J. M. Tomlinson, D. R. Collins, M. J. Cubison, E .J. Dunlea, J. A. Huffman, T. B. Onasch, M. R. Alfarra, P. I. Williams, K. Bower, Y. Kondo, J. Schneider, F. Drewnick, S. Borrmann, S. Weimer, K. Demerjian, D. Salcedo, L. Cottrell, R. Griffin, A. Takami, T. Miyoshi, S. Hatakeyama, A. Shimono, J.Y Sun, Y. M. Zhang, K. Dzepina, J. R. Kimmel, D. Sueper, J. T. Jayne, S. C. Herndon, A. M. Trimborn, L. R. Williams, E. C. Wood, C. E. Kolb, U. Baltensperger, D. R. Worsnop

*To whom correspondence should be addressed. E-mail: jose.jimenez@colorado.edu (J.L.J.); andre.prevot@psi.ch (A.S.H.P.)

Published 11 December 2009, *Science* **326**, 1525 (2009)
DOI: 10.1126/science.1180353

This PDF file includes:

Supporting Online Material for
Evolution of Organic Aerosols in the Atmosphere

J.L. Jimenez[1]*, M.R. Canagaratna[2], N.M. Donahue[3], A.S.H. Prevot[4]*, Q. Zhang[5,6], J.H. Kroll[2,7], P.F. DeCarlo[1,4,8], J.D. Allan[9,10], H. Coe[9], N.L. Ng[2], A.C. Aiken[1+], K.D. Docherty[1], I.M. Ulbrich[1], A.P. Grieshop[3++], A.L. Robinson[3], J. Duplissy[4#], J. D. Smith[11], K.R. Wilson[11], V.A. Lanz[4,12], C. Hueglin[12], Y.L. Sun[5,6], J. Tian[5], A. Laaksonen[13,14], T. Raatikainen[13,14], J. Rautiainen[13], P. Vaattovaara[13], M. Ehn[15], M. Kulmala[15,16], J.M. Tomlinson[17##], D.R. Collins[17], M.J. Cubison[1] , E.J. Dunlea[1=], J.A. Huffman[1==], T.B. Onasch[2],M.R. Alfarra[4,9,10], P.I. Williams[9,10], K. Bower[9], Y. Kondo[18], J. Schneider[19], F. Drewnick[5,19], S. Borrmann[19,20], S. Weimer[5,21], K. Demerjian[5], D. Salcedo[22], L. Cottrell,[23x] R. Griffin[23,24], A. Takami[25], T. Miyoshi[25xx], S. Hatakeyama[25&], A. Shimono[26] J.Y Sun[27], Y.M. Zhang[27], K. Dzepina,[1,28&&], J.R. Kimmel[1,2,29], D. Sueper[1,2], J.T. Jayne[2], S.C. Herndon[2], A.M. Trimborn[2], L.R. Williams[2], E.C. Wood[2], C.E. Kolb[2], U. Baltensperger[4], and D.R. Worsnop[2,13,15]

1. Cooperative Institute for Research in the Environmental Sciences (CIRES) and Dept. Chemistry and Biochemistry, Univ. of Colorado, Boulder, CO, USA
2. Aerodyne Research, Inc. Billerica, MA, USA
3. Center for Atmospheric Particle Studies, Carnegie Mellon University, Pittsburgh, PA, USA
4. Laboratory of Atmospheric Chemistry, Paul Scherrer Institut, Villigen, Switzerland,
5. Atmospheric Sciences Research Center, State University of New York, Albany, NY, USA
6. Department of Environmental Toxicology, University of California, Davis, CA, USA
7. Dept. Civil Environ. Eng., Massachusetts Institute of Technology, Cambridge, MA, USA
8. Dept. of Atmos. Ocean. Sci., Univ. of Colorado, Boulder, CO, USA
9. School of Earth, Atmos., and Environ. Sci., University of Manchester, Oxford Road, Manchester, UK
10. National Centre for Atmospheric Science, University of Manchester, Oxford Road, Manchester, UK
11. Chemical Sciences Division, Lawrence Berkeley National Laboratory, Berkeley, CA, USA
12. Empa, Laboratory for Air Pollution/Environmental Technology, Dübendorf, Switzerland
13. Dept. of Physics, University of Kuopio, Kuopio, Finland
14. Finnish Meteorological Institute, Helsinki, Finland
15. Dept. of Physics, University of Helsinki, Helsinki, Finland
16. Dept. of Applied Environmental Science, Stockholm University, Stockholm, Sweden
17. Dept. of Atmospheric Sciences, Texas A&M University, College Station, TX, USA
18. Research Center for Advanced Science and Technology, University of Tokyo, Tokyo, Japan
19. Particle Chemistry Department, Max Planck Institute for Chemistry, Mainz, Germany
20. Institute for Atmospheric Physics, Johannes Gutenberg University, Mainz, Germany
21. Empa, Laboratory for Internal Combustion Engines, Dübendorf, Switzerland
22. Centro de Investigaciones Quimicas, Univ. Autonoma del Estado de Morelos, Cuernavaca, Mexico
23. Climate Change Research Center, Univ. of New Hampshire, Durham, NH, USA
24. Dept. of Civil and Environmental Engineering, Rice University, Houston, TX, USA
25. Asian Environmental Research Group, National Institute for Environmental Studies, Tsukuba, Japan
26. Sanyu Plant Service Co. Ltd., Sagamihara, Japan
27. Key Laboratory for Atmos. Chem., Chinese Academy of Meteorological Sciences, Beijing, China
28. Atmospheric Chemistry Division, National Center for Atmospheric Research, Boulder, CO, USA
29. Tofwerk AG, Thun, Switzerland

*: Corresponding authors (jose.jimenez@colorado.edu, andre.prevot@psi.ch)
+: now at the Swiss Federal Institute of Technology, Zurich, Switzerland
++: now at Institute for Resources, Environ. & Sustainability, U. of British Columbia, Vancouver, Canada
#: now at CERN, Geneva, Switzerland;
##: now at Pacific Northwest National Laboratory, Richland, WA, USA
=: now at Climate Program Office, NOAA, Silver Spring, MD, USA
==: now at Department of Biogeochemistry, Max Planck Institute for Chemistry, Mainz, Germany
x: now with Environ International Corporation in Groton, Massachusetts
xx: now at Tokyo Metropolitan Research Institute for Environmental Protection, Tokyo, Japan
&: now at Institute of Symbiotic Science and Technology, Tokyo Univ. of Agriculture and Technology
&&: now at Particle Chemistry Department, Max Planck Institute for Chemistry, Mainz, Germany

Section S1. Materials and Methods

S1.1. Description of Laboratory Aging Experiments

The α-pinene SOA and squalane aging experiments shown in Figures 2c-d were conducted at the Advanced Light Source at the Lawrence Berkeley National Laboratory in Berkeley, California *(S1, S2)*. SOA from α-pinene ozonolysis is generated by mixing α-pinene (~40 ppm, from bubbling N_2 through α-pinene) with ozone (~500 ppb, generated by passing N_2/O_2 mixture through a quartz absorption cell illuminated by a pen-ray Hg lamp) in a 130 cm long, 2.5 cm ID flow tube. The total residence time within the flow tube is ~90 s, which is sufficient to generate a high concentration of SOA particles. Upon exiting the flow tube the aerosol stream is passed through a carulite ozone denuder and an activated carbon trap to remove any remaining ozone, α-pinene, and gas phase organic products. In a separate oven, squalane aerosol is formed by homogeneous nucleation of the heated vapor above a liquid sample.

The heterogeneous oxidation of either α-pinene SOA or squalane particles by OH radicals is carried out in a second flow tube (130 cm long, 2.5 cm ID, type 219 quartz). The aerosol stream is mixed with humidified N_2 (RH = 10-60%, controlled by a water bubbler), O_2 (5%), and variable amounts of O_3 (generated by passing pure O_2 through a corona discharge). OH radicals are generated within the reaction cell by the photolysis of ozone using light from four 130 cm long Hg (λ = 254 nm) lamps (UVP, Upland, CA) positioned along the length of the reactor, followed by reaction with water vapor. OH concentration is varied by adjusting both the RH and ozone concentration within the flow cell. The steady state OH concentrations are estimated using a kinetic modeling program fit to GC-FID measurements of the decay of hexane over a large range of precursor, RH, and ozone concentrations. The total flow through the reactor is 1.0 L min^{-1}, which corresponds to an exposure time of ~ 37 s. The temperature of the reactor was ~35^{o}C as a result of moderate heating from the nearby UV lamps. As discussed by Smith et al. (2009), the heterogeneous reaction rate should be only very weakly dependent on temperature, and therefore the effect of the 10^{o}C difference from room temperature should be insignificant for those experiments. Upon exiting the reactor a portion of the aerosol stream is sampled by an Aerodyne HR-ToF-AMS *(S3)*. The remainder of the aerosol stream is sent to a differential mobility analyzer (DMA) and condensation particle counter (CPC) to measure the size and concentration of the particles.

The aging experiments for diesel and biomass burning emissions shown in Figures 2e-f were carried out in the smog chamber at Carnegie Mellon University. Briefly, source emissions were injected into the smog chamber and, after an initial mixing period, photochemical aging was driven using UV lights. Further experimental details are described by *(S4-S7)*. A quadrupole AMS (Q-AMS) *(S8-S9)* was used to characterize the evolving OA composition.

S1.2. Experiments Relating Hygroscopic Growth to O:C of Organic Aerosols

Figure 3 summarizes the results of several laboratory and field experiments, which are summarized in this section.

Smog chamber experiments. The hygroscopic properties of laboratory generated SOA were measured at the PSI environmental reaction chamber *(S10)*. Photochemical

reactions in a mixture of hydrocarbons and NO_x were induced by light which leads to the formation of oxygenated volatile organic compounds and concurrently to SOA. First, the chamber (27 m^3) was humidified to ~50% nominal relative humidity. Then NO and NO_2 were added sequentially. Next, a small amount of a liquid hydrocarbon (1,3,5-trimethylbenzene (TMB), α-pinene or isoprene) was injected into a heated glass bulb which was then flushed into the chamber with pure air produced by a zero air generator (AADCO 737-series 15 A). The compounds were left to mix in the chamber for approximately 15-30 minutes before turning on the 4 xenon lamps (4 kW each). Initial input concentrations for the experiments are presented in Table S1. Growth factors (GF), defined as the ratio of droplet size at a given relative humidity (RH) to the dry size depend on the hygroscopic properties of the aerosol components. Growth factors were measured using a hygroscopicity tandem differential mobility analyzer (HTDMA). Briefly, a narrow size distribution of dried particles (<10% RH) is selected, particles are exposed to water at a fixed elevated RH and the final size distribution is measured. The HTDMA used in this study is described in *(S11)* and was operated at an RH of 95%. The residence time of the aerosol at the chosen RH prior to entering the second DMA was 15 s. The effective hygroscopicity parameter was estimated here and for the rest of the experiments described in this section with the method of Petters and Kreidenweis *(S12)*. A Q-AMS was used to characterize the OA composition *(S8-S9)*, and O:C was estimated using the methods in *(S13)*.

Field Measurements at the high-alpine site Jungfraujoch (JFJ). The JFJ is a European high-alpine background site located on an exposed mountain ridge in the Bernese Alps, Switzerland, at 3580m altitude (46.33º N, 7.59º E). The station is surrounded by glaciers and rocks, and no local vegetation is present. Within the World Meteorological Organization (WMO) Global Atmosphere Watch (GAW) program continuous measurements of aerosol parameters have been performed at the JFJ site since 1995 *(S14)*. Hygroscopicity and AMS measurements were performed during the Cloud and Aerosol Characterization Experiment (CLACE3) from February to April 2004. The HTDMA used in this study is described in *(S15)* and was used to measure the diameter increase from RH <10% to RH of 85%. The residence time of the aerosol at the chosen RH prior to entering the second DMA was 20 s. Since ambient aerosol contained inorganic species and black carbon besides OA, the hygroscopic growth due to OA only was extracted using the Zdanovskii-Stokes-Robinson (ZSR) method *(S16)*. To compare GF values measured at different RH, we used the semi-empirical model described in Petters and Kreidenweis *(S12)*. The same Q-AMS described above for the PSI smog chamber experiments was used here.

Mexico City Field measurements. The Megacity Initiative: Local and Global Research Observations (MILAGRO) took place in and around Mexico City during March 2006. The MILAGRO campaign was designed to study the chemical characterization and transformation of pollutants from the Mexico City urban area to regional and global scales. A HR-ToF-AMS *(S3)* and a HTDMA were deployed on an aircraft platform onboard the National Science Foundation/National Center for Atmospheric Research (NSF/NCAR) C-130 aircraft. Details on the AMS deployment and general results for the campaign are described in *(S17)*. The HTDMA used in this study is described in *(S18)* and was operated between RH <10% and RH of 85%. The residence time of the aerosol at the chosen RH prior to entering the second DMA was 10 s.

Field Measurements at the Hyytiälä Forested Site. Figure 3 also shows two points (labeled "Hyytiälä LV-OOA" and "Hyytiälä SV-OOA") summarizing the results from a field study at the Hyytiälä Forestry Station in Finland which took place during the spring 2005 BACCI (Biosphere-Aerosol-Cloud-Climate Interactions) and QUEST (Quantification of Aerosol Nucleation in the European Boundary Layer) field experiments. A Q-AMS was operated alongside three TDMA instruments measuring the change in diameter of dried ambient particles exposed to water vapor (hygroscopicity, HTDMA) *(S19)*, ethanol vapor (organic affinity, OTDMA) *(S20,S21)*, or heat (volatility, VTDMA) *(S22)*. The HTDMA and OTDMA were operated at saturation ratios of about 0.88 and 0.82, respectively. Growth factors were measured for different dry particle diameters, but only 50 nm data are used here as it is the largest size measured by the TDMAs and closest to the smallest particle sizes observed with the AMS. Residence times were 1-2 s which are sufficient for particles of these small sizes *(S23)*.

Only two organic factors, LV-OOA and SV-OOA, were found when the measured organic mass spectrum was analyzed by the positive matrix factorization (PMF) technique *(S24-S26)*, and their relative volatilities were confirmed with the VTDMA. Most of the variability in hygroscopic and ethanol growth factors (HGF and EGF, respectively) was captured by a simple model. Volume fractions (v_i) of the main inorganic ions (SO_4+NH_4+NO_3) and the two organic groups of species (LV-OOA and SV-OOA) were calculated. Hygroscopic and ethanol growth factors (HGF and EGF, respectively) of the three groups were treated as fitting parameters, when the equations:

$$HGF^3 = v_{inorg} \times HGF^3_{inorg} + v_{LV\text{-}OOA} \times HGF^3_{LV\text{-}OOA} + v_{SV\text{-}OOA} \times HGF^3_{SV\text{-}OOA} + \varepsilon_H$$

$$EGF^3 = v_{inorg} \times EGF^3_{inorg} + v_{LV\text{-}OOA} \times EGF^3_{LV\text{-}OOA} + v_{SV\text{-}OOA} \times EGF^3_{SV\text{-}OOA} + \varepsilon_O$$

were fitted to the experimental data; ε_i are the residuals of the fits. These fits produced six parameters, i.e. hygroscopic and ethanol growth factors for each group. The fitted growth factors, which are given in Table S2, are indicative of average properties of the groups. In general, the measured HGF and EGF values correlate with the expected solubility of these groups in water and ethanol. Inorganic species have high hygroscopic growth factors and low ethanol growth factors. LV-OOA, has a moderate HGF that is consistent with the fact that it is highly oxidized and a moderate EGF that is consistent with its organic composition. The less oxidized SV-OOA is insoluble in water at 88 % relative humidity, but it has the highest EGF. This simple model with three component groups provided the best fit to the measured HGF and EGF values. When total OA was considered as a single component, the fitting performed significantly worse during many time periods. Similarly, increasing the number of organic groups extracted from PMF did not improve the fits for time periods with the lowest correlations. The fact that both particle hygroscopicity and organic affinity – two different physicochemical properties – can be parameterized using the concentrations of SV-OOA and LV-OOA, shows clearly that these are relevant groups of organic species with different average physicochemical properties, and not merely mathematical constructions produced by the factor analysis.

S1.3. Description of the Model of SOA Formation and Aging.

The modern understanding of secondary organic aerosol builds on the foundation laid by Pankow (1994) *(S27)* and Odum *et al.* (1997) *(S28)*, which describes the phase

partitioning of semivolatile organic mixtures. Recent studies of primary emissions have also revealed that primary emissions behave as we expect semivolatile mixtures to behave, evaporating upon dilution as the system works to maintain a constant vapor pressure *(S29)* and also evaporating substantially upon mild heating *(S30,S31)*. A key conclusion from these studies is that there is a very substantial pool of organic mass in the vapor phase in equilibrium with the primary organic particles *(S32-33)*. The phase partitioning of this mixture is driven by the mass concentration of organic aerosol (C_{OA}) distributed over 'bins' described by their saturation concentration (C^*) at 298 K; this is the foundation of the volatility basis set (VBS) *(S32)*. The mass fraction F_i in the condensed phase in each bin i with volatility C_i^* is given by

$$F_i = (1 + C_i^*/C_{OA})$$

as described by Donahue *et al. (S32)*. The temperature dependence of partitioning is fully described by the Clausius Clapeyron equation; changing temperatures cause the C_i^* bins to shift from their nominal 298K value to higher or lower values as temperature increases or decreases from 298 K *(S32, S34)*.

These vapors will react with OH radicals in the gas phase, often with a rate constant near 3×10^{-11} cm^3 $molec^{-1}$ s^{-1} *(S35)*. Heterogeneous reactions of OH with particles can also play a role, but mass-transfer limitations restrict them to be a factor of 3-10 slower than gas-phase oxidation of these vapors *(S36)*. In either case, the critical question is what the reaction products will be and whether they will have lower or higher C^* values than the precursor.

In addition to changing the C^* values, reactions will change the oxygen content of the organic compounds. The chemical composition of material with a given C^* value is largely controlled by the oxygen to carbon ratio (O:C) of the compounds, and the composition can vary widely depending on this parameter. For example, material in the 1 μg m^{-3} bin can range from C_{25} alkanes to simple sugars ($C_6O_6H_x$). There are tens of thousands of organic structures with 10 or so carbons and varying numbers of oxygen atoms (not to mention H and N). However, structure activity relationships (SAR) such as those recently described by Pankow and Asher (2008) *(S37)* reduce the broad effects of added oxygen moieties to some simple rules: added -OH functionality decreases the C^* of an organic backbone by a factor of about 100 (180), while added =O functionality decreases C^* by 10. Based on these simple rules as well as C^* values for alkanes and a few oxygenated compounds, we have developed a 2-dimensional VBS (2D-VBS), adding O:C as a 2^{nd} dimension to complement C^*. Another 2D-VBS has recently been proposed based on carbon number and polarity, which however are not directly characterizable experimentally for the total OA in either ambient or chamber experiments *(S38)*. C^* and O:C are fundamentally empirical quantities, but we can relate them to properties predicted from thermodynamic theory and SARs. Moreover, since high time-resolution experimental measurements are now available for both of these properties, the model framework can be experimentally constrained and verified with both laboratory and field measurements.

For use in a box model, we use C^* ranging from 10^{-5} to 10^9, separated by powers of 10, and O:C ranging from 0 to 1, separated by 0.1. The bins with $C^* >\sim 10^6$ are included only to consider the phenomenology; any complete model would explicitly model the VOCs

and oxygenated VOCs (OVOCs) in that range. We can predict the average properties in each of the 165 bins. For example, C^* = 1 μg m^{-3} and O:C = 0 is roughly C_{25}, while C^* = 1 μg m^{-3} and O:C = 0.4 is roughly C_{10} ($C_{10}O_4H_x$). Application in 3-D models will require a substantially coarser distribution of bins, and representing only those portions of the space where a substantial fraction of the mass evolves.

To simulate the chemistry of vapors in the 2D-VBS, we have constructed two 'oxidation kernels' describing two competing processes, functionalization and fragmentation, depicted in Figure 4c. Functionalization is formation of a product with an identical carbon number but increased O:C, while fragmentation is formation of at least two products with lower carbon numbers (as well as an increased O:C for the aggregate). In the 2-D VBS we track carbon mass and compute the total organic mass to simplify mass conservation. The functionalization kernel assumes that each generation of oxidation by OH that does not cause fragmentation reduces C^* by between 1 and 6 decades and adds between 1 and 3 oxygen atoms (with the change in O:C depending on the mean carbon number of a given starting bin). A key simplifying assumption is that reactions in the functionalization branch will be similar for all bins in the 2D-VBS. The functionalization behavior is represented by the functionalization kernel shown in Figure S2; distributing the products in the x direction (C^*) is straightforward, while the y-direction (O:C) depends on the average carbon number of the starting bin, which is known. The functionalization matrix at present is designed to depict typical changes under low-NO_x conditions; treatment of high-NO_x chemistry will require a parallel set of bins representing organic nitrates.

We hypothesize that the major difference in mechanisms for different compounds (represented by different bins) is a changing ratio of functionalization to fragmentation. A second key assumption is that this branching ratio (β) can be represented by a simple function of O:C - specifically $(O:C)^n$. For the results shown here we have assumed $\beta = (O:C)^{(1/6)}$. This means that compounds with an O:C of 0.5 have a 90% chance of fragmenting. For fragmentation, we assume that the C-C bond that cleaves is randomly distributed along the carbon backbone. This means that the carbon mass in the products is a triangular distribution weighted toward the heavy products. We assume that this applies to C^* bins more volatile than a given precursor. For example, if a precursor with C^*=1 μg m^{-3} fragments, the 10 μg m^{-3} bin will receive the most carbon mass, and the 10^9 bin the least, with a normalized distribution. As a simplification, we assume that the bins to the left of the midpoint have an unchanged O:C, while the bins to the right of the midpoint (more volatile) progress diagonally toward the bin (10^9,1). The resulting fragments are then processed with a similar oxidation kernel to the one shown above, with the major difference being that many heavy fragments are assumed to end up with roughly the same O:C as the precursor compound. Fragmentation is represented in Figure S3 and thus fills the wide area in the fragmentation region shown in Figure 4. This simple representation is designed only to capture the barest key features of the fragmentation process.

Figures S2 and S3 below depict the functionalization and fragmentation branches in our 2D VBS for a bin at 100 μg m^{-3} and an O:C of 0.4 (averaging roughly 9 carbons and 3.5 oxygens). Functionalizaton reactions out of this bin generate products in the bins with probabilities as shown; the most likely result (16% of the carbon) is a decrease in C^* by 3

decades and an increase in O:C of 0.2. However, the products spread through the range of expected fuctionalities as indicated by the dashed red lines (similar to Figure 4). The fragmentation reactions disperse material over a much wider range in the 2D space, as fragmentation is assumed to occur more or less randomly along the C-C backbone (given that there may be 100s of C_9O_4 isomers represented by the bin, and even the carbon number will range from C_7 to C_{12}). However, the majority of the products are found with a slight increase in *C** and either no change or a modest increase in O:C.

Heterogeneous uptake of OH onto particles will also oxidize organics. Field evidence *(S17, S39)* and laboratory aging of ambient particles *(S40)* indicate this is a minor pathway. Experimental evidence is scant, but it appears that the functionalization vs. fragmentation issues are similar. At present we model heterogeneous oxidation with the same kernels. With an assumed gas-phase rate constant with OH of about 3×10^{-11} cm^3 $molec^{-1}$ s^{-1} and an assumed uptake coefficient of 1.0 *(S36)*, the heterogeneous rate of carbon oxidation is at least a factor of 10 slower than the homogeneous rate. This "heterogeneous slowdown" is a critical feature of the framework, as it means that organic material is somewhat sheltered from oxidation by gas-phase OH when it resides in the condensed phase. Gas-phase rate constants may slow somewhat with increasing oxidation (for example in the series from pinonaldehyde to pinonic acid to pinic acid the OH rate constant at 298 K decreases from 3.5×10^{-11} cm^3 $molec^{-1}$ s^{-1} to 0.9×10^{-11} cm^3 $molec^{-1}$ s^{-1} *(S35)*), but the largest uncertainty in these simulations is the fragmentation branching ratio β.

We have implemented these features in a simple box model, starting with a mass-conserving distribution of α-pinene + ozone reaction products. The volatility of the initial products is constrained by chamber data showing aerosol formation *(S33)*. In addition, a systematic relationship has been reported between increasing O:C and decreasing total SOA mass *(S41-S42)*, further supporting that the more highly oxidized reaction products also have lower *C** values (as discussed above). Combining constraints on the *C** distribution from aerosol yields vs. SOA concentrations, the average O:C vs. SOA concentrations, and a requirement that most of the products have 10 or 9 carbons, we obtain a tight and self-consistent constraint on the 2-D product distribution from this reaction. This is shown with the blue contours (0.70 and 0.125 of the maximum) in Figure 4, extending from α-pinene, which is a green circle. The large majority of the carbon mass has a *C** between 10^4 and 10^6 μg m^{-3} with an O:C between 0.2 and 0.1. However, a tail in the distribution extends down to 1 μg m^{-3} and an O:C of 0.4.

The simple box model takes no account of differing kinetics other than the ratio of homogeneous to heterogeneous oxidation; instead it is run in non-dimensional time units tied to a (uniform) gas-phase lifetime. For a typical rate constant of 3×10^{-11} cm^3 $molec^{-1}$ s^{-1} and a typical mid-day OH concentration of 6×10^6 molec cm^{-3}, one "lifetime" corresponds to about 1.5 hours, so this chemistry will occur very quickly. Future work will focus on more realistic representation of kinetics and mechanisms, especially with regard to the fragmentation and oligomerization pathways. Oligomerization is not currently modeled in this framework because the research community is far from a consensus on the fraction of condensed-phase organic compounds or the key mechanisms involved in oligomerization chemistry. As these aspects are clarified by further research, oligomerization chemistry can be added to this 2D-VBS framework.

Figures for Supplementary Online Material

Figure S1. High-resolution spectra derived from Positive Matrix Factorization (PMF *(S24-S26)*) analysis of ground-based data of two field studies in Riverside, California in Jul.-Aug. 2005 as part of the SOAR-1 campaign *(S43)*, and Mexico City in March 2006 as part of the MILAGRO campaign *(S13)*. HOA: hydrocarbon-like organic aerosol; SV-OOA: semivolatile oxygenated organic aerosol; LV-OOA: low-volatility oxygenated organic aerosol; Local OA: local organic aerosol; BBOA: biomass burning organic aerosol.

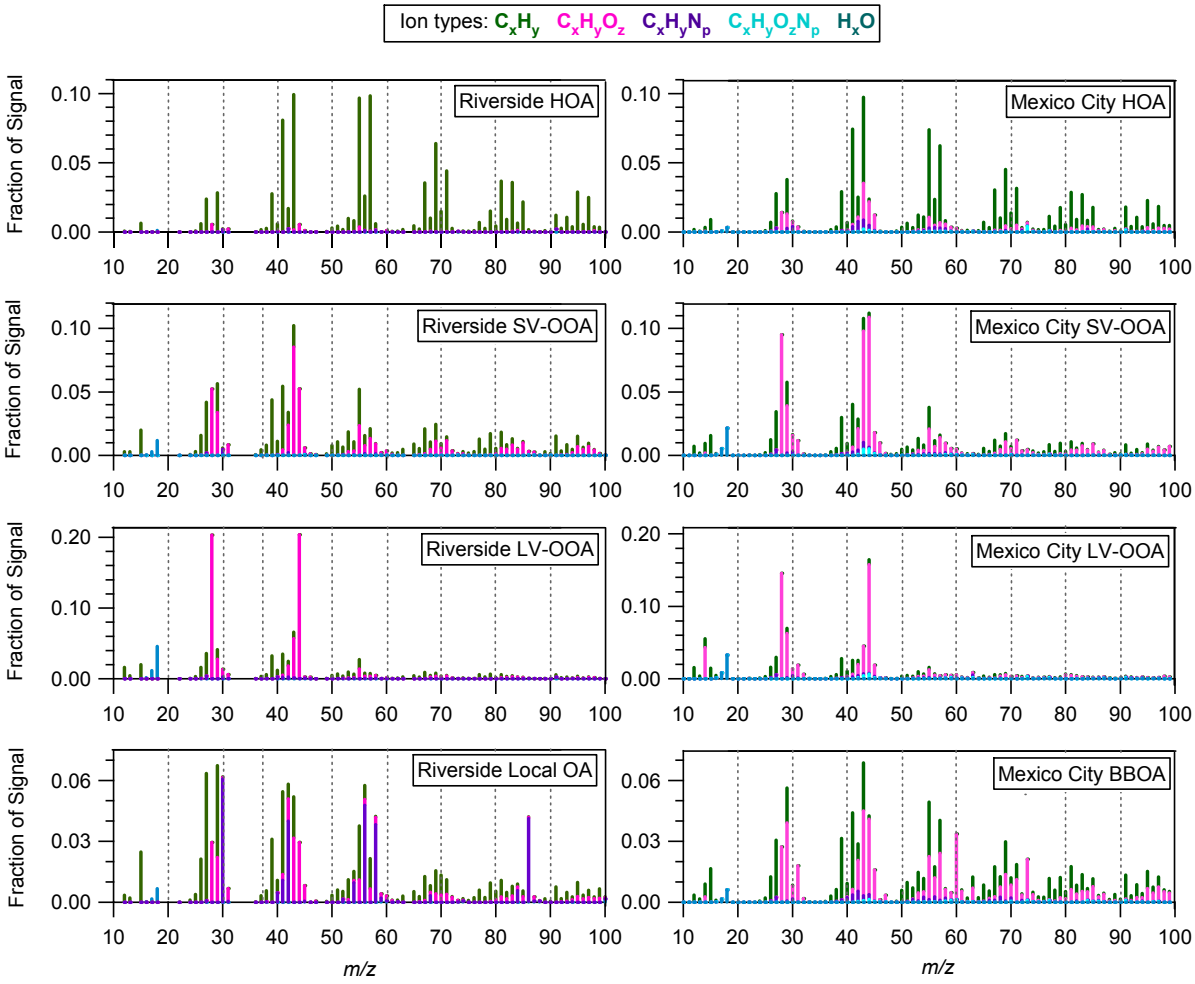

Figure S2. Representation of the functionalization pathway used in the 2D-VBS model. Reactions out of the bin (2,0.4:1) (green circle, nominal $C_9O_{3.6}$) generate products with the probabilities (yields) shown. Concentrations in all bins are carbon mass concentration, and the yields sum to 1.0, so carbon is conserved. The most probable reactions add 1, 2 or 3 oxygens with C^* dropping by about 1.5 (in log space) per added O.

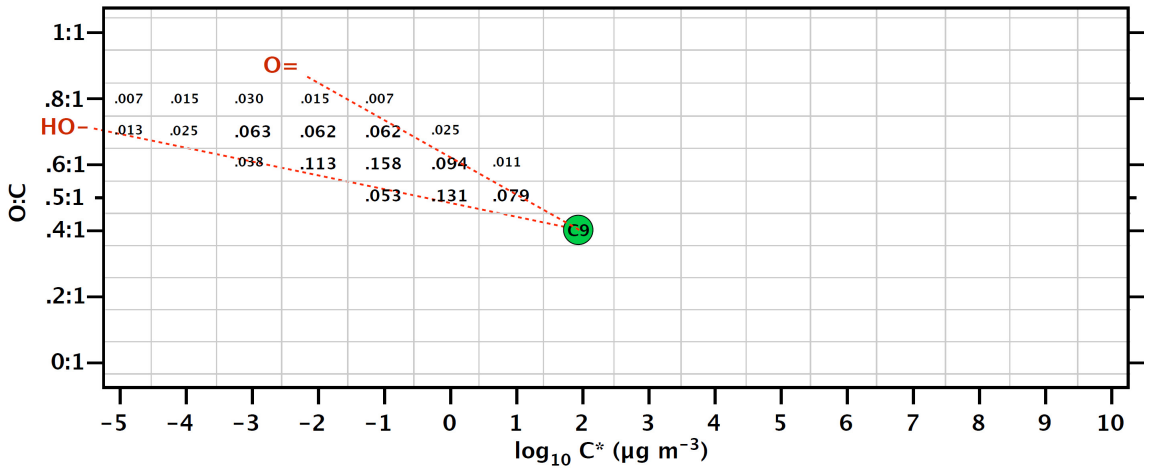

Figure S3. Representation of the fragmentation pathway used in the 2D-VBS model. Fragmentation out of the same bin as Figure S2 (2,0.4:1) (green circle, nominal $C_9O_{3.6}$) generates products with lower nominal carbon numbers dispersed over a wide area in the *C** space. The distribution is derived from two premises: First, fragmentation is assumed to be at a randomly selected C-C bond, meaning that for a C10 precursor there will be equal *molar* yields of C_9, C_8, ... C_1 products. The mass yield distribution is *triangular,* favoring C_9. Second, the resulting fragments are assumed to add 0, 1, or 2 oxygens relative to the O:C of the parent. Product carbon yields are thus largest near the parent, with wide distribution, some products have substantially decreased *C** in spite of reduced carbon number, consistent with the C_8 triacid product shown in Figure 4.

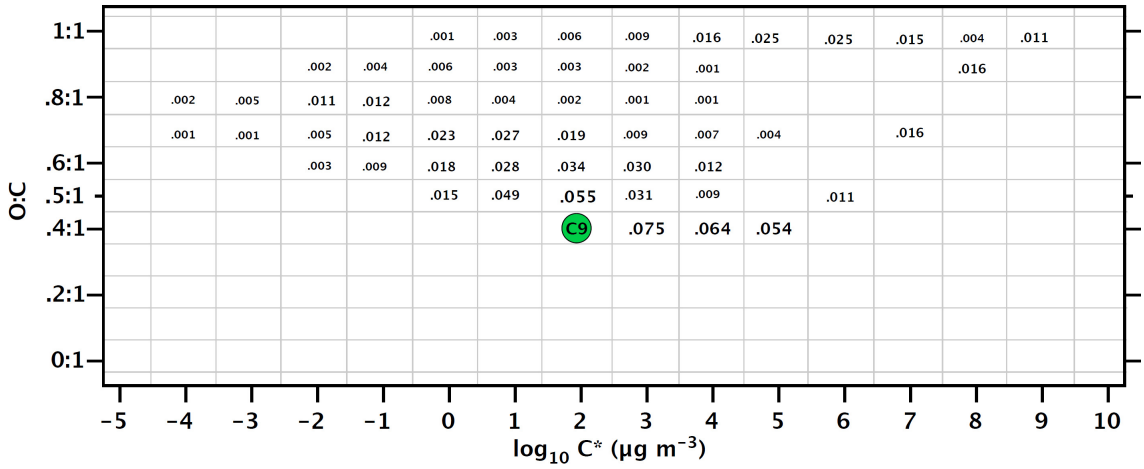

Tables for Supplementary Online Material

Table S1: Experimental conditions for SOA formed at the smog chamber.

Experiment	Precursor	Precursor concentration [ppb]	NO[ppb]	NO_2[ppb]	r^2 between κ and O:C
1	TMB	150	-	75	0.97
2	TMB	86	-	43	0.92
3	α-pinene	180	48	60	0.92
4	α-pinene	124	31	41	0.94
5*	α-pinene	10	-	5	*0.67*
6	isoprene	1200	300	300	0.95

* Experiment 5 is a combination of two similar experiments where the AMS and HTDMA were not measuring simultaneously.

Table S2. Fitted hygroscopic (HGF) and ethanol (EGF) growth factors for the three groups at saturation ratios (S) of 0.88 and 0.82, respectively.

	HGF @ S = 0.88	EGF @ S = 0.82
$SO_4 + NH_4 + NO_3$	1.53	1.00
LV-OOA	1.29	1.12
SV-OOA	1.00	1.16

Table S3: Location, duration, season, previous publications, and acknowledgements for the field studies shown in Figure 1. These tables are also included as a Microsoft Excel (.xls) file as part of the SOM of this paper.

Location	Field Campaign	Site type	Coordinates		Time Period	Duration	Season	Previous Publications	Funding Acknowledgements for Individual Studies
			Long.	Lat.					
Beijing, China		Urban	116.0	40.0	7/9/2006 - 7/21/2006	12 days	Su	*Sun et al.* [2009] *(S44)*	NNSF of China 40575063, NBRP of China 2006CB403703 & 2006CB403701, US NSF ATM-0840673, US DOE DE-FG02-08ER64627
Tokyo, Japan		Urban	139.75	35.67	7/23/2003 - 8/14/2003	23 days	Su	*Takegawa et al.* [2005, 2006] *(S45,S46)*	MEXT and JST
Tokyo, Japan		Urban	139.75	35.67	1/20/2004 - 2/10/2004	20 days	W	*Takegawa et al.* [2005, 2006] *(S45,S46)*	MEXT and JST
Pittsburgh, PA, USA	PAQS	Urban	-79.94	40.44	9/6/2002 - 9/22/2002	15 days	F	*Zhang et al.* [2004, 2005abc, 2007] Ulbrich et al. [2009] *(S26,S47-S51)*	NSF ATM-0449815, NASA NNG04GA67G
Mexico City, Mexico	MILAGRO	Urban	-99.15	19.48	3/10/2006 - 3/30/2006	21 days	Sp	*Aiken et al.* [2008, 2009] *(S13,S52)*	NSF ATM-0513116 & ATM-0528634, DOE DE-FG02-05ER63981
Riverside, CA, USA	SOAR-1	Urban	-117.40	33.95	7/14/2005 - 8/13/2005	30 days	Su	*DeCarlo et al.* [2006], *Docherty et al.* [2008], Cubison et al. [2008] *(S3,S43,S53)*	EPA RD-83216101-0, EPA STAR R831080, NSF ATM-0513116
Houston, TX, USA	TexAQS-2000	Urban	-95.36	29.76	8/15/2000 - 9/15/2000	31 days	Su - F	*Tanaka et al.* [2003] *(S54)*	State of Texas
Boulder, CO, USA	BFS	Urban	-105.27	40.02	6/7/2003 - 6/20/2003	14 days	Su	*Nemitz et al.* [2008] *(S55)*	EPA RD-83216101-0, NSF ATM-0513116, NASA NNG04GA67G
New York City, USA	PMTACS	Urban	-73.82	40.74	6/30/2001 - 8/5/2001	36 days	Su	*Drewnick et al.* [2004a, b] *(S56-S57)*	NYS DEC C004210, NYSERDA 4918ERTERE-S99 and US EPA R828060010
New York City, USA	PMTACS	Urban	-73.82	40.74	1/7/2004 - 2/6/2004	30 days	W	*Weimer et al.* [2006] (*S58)*	NYS DEC C004210, NYSERDA 4918ERTERE-S99
Vancouver, Canada	PACIFIC-2001	Urban	-123.13	49.25	8/11/2001 - 8/24/2001	13 days	Su	*Boudries et al.* [2004], *Alfarra et al.* [2004] *(S59-S60)*	Environment Canada, GBEI, and PERD
Edinburgh, UK		Urban	-3.20	55.95	10/31/2000 - 11/10/2000	10 days	F	*Allan et al.* [2003ab] *(S61-62)*	UK NERC GR3/12499 & NER/S/A/2000/03653
Manchester, UK		Urban	-2.22	53.50	6/14/2001 - 6/25/2001	11 days	Su	*Allan et al.* [2003ab] *(S61-62)*	UK NERC GR3/12499 & NER/S/A/2000/03653
Manchester, UK		Urban	-2.22	53.50	1/17/2002 - 1/28/2002	11 days	W	*Allan et al.* [2003ab] *(S61-62)*	UK NERC GR3/12499 & NER/S/A/2000/03653
Mainz, Germany		Urban	8.23	49.98	9/16/2004 - 10/1/2004	15 days	F	*Vester et al.* [2007] *(S63)*	Deutsche Forschungsgemeinschaft
Zurich, Switzerland		Urban	8.50	47.40	7/14/2005 - 8/4/2005	21 days	Su	Lanz et al. [2007] *(S25)*	Swiss Federal Office for the Environment (FOEN)
Zurich, Switzerland		Urban	8.50	47.40	1/6/2006 - 1/25/2006	19 days	W	Lanz et al. [2008] *(S64)*	Swiss Federal Office for the Environment (FOEN)
Cruise track along East coast of USA, Leg1	NEAQS-2002	Urban Downwind	-78.1 ~ -70.5	32.8 ~ 43.1	7/18/2002 - 7/26/2002; 7/29/2002 - 8/10/2002	21 days	Su	*deGouw et al. [2005], Marcolli et al.* [2007], *Bates et al.* [2005] (*S65-67)*	NOAA
Chelmsford, UK	TORCH-1	Urban Downwind	0.42	51.74	7/29/2003 - 8/31/2003	33 days	Su	*Cubison et al.* [2006] *(S68)*	UK NERC PTP
Taunus, Germany		Urban Downwind	8.45	50.22	7/14/2004 - 8/4/2004	21 days	Su	*Dusek et al.* [2006], *Hings et al.,* [2007] *(S69-S70)*	MPI and Univ. of Mainz

Location	Field Campaign	Site type	Coordinates		Time Period	Duration	Season	Previous Publications	Funding Acknowledgements for Individual Studies
			Long.	Lat.					
Fukue Island, Japan		Rural / Remote	128.84	32.69	3/18/2003 - 4/3/2003	16 days	Sp	*Takami et al.* [2005] *(S71)*	GERF/MoE (B-8), JST-CREST(APEX), MEXT (AIE 416)
Fukue Island, Japan		Rural / Remote	128.84	32.69	4/3/2003 - 4/16/2003	13 days	Sp	*Takami et al.* [2005] *(S71)*	GERF/MoE (B-8), JST-CREST(APEX), MEXT (AIE 416)
Fukue Island, Japan		Rural / Remote	128.84	32.69	5/10/2003 - 6/3/2003	24 days	Sp - Su	*Takami et al.* [2005] *(S71)*	GERF/MoE (B-8), JST-CREST(APEX), MEXT (AIE 416)
Okinawa Island, Japan		Rural / Remote	128.25	26.87	10/3/2003 - 10/28/2003	25 days	F	*Miyoshi et al.* [2009] *(S72)*	GERF/MOE (C-51), MEXT (W-PASS 462)
Okinawa Island, Japan		Rural / Remote	128.25	26.87	10/28/2003 - 12/2/2003	35 days	F - W	*Miyoshi et al.* [2009] *(S72)*	GERF/MOE (C-51), MEXT (W-PASS 462)
Okinawa Island, Japan		Rural / Remote	128.25	26.87	12/2/2003 - 12/24/2003	22 days	W	*Miyoshi et al.* [2009] *(S72)*	GERF/MOE (C-51), MEXT (W-PASS 462)
Okinawa Island, Japan		Rural / Remote	128.25	26.87	3/13/2004 - 4/8/2004	26 days	Sp	*Miyoshi et al.* [2009] *(S72)*	GERF/MoE (B-8, C-51), MEXT (AIE 416)
Okinawa Island, Japan		Rural / Remote	128.25	26.87	4/8/2004 - 4/27/2004	19 days	Sp	*Miyoshi et al.* [2009] *(S72)*	GERF/MoE (B-8, C-51), MEXT (AIE 416)
Cheju Island, Korea	ACE-Asia	Rural / Remote	126.50	33.51	4/11/2001 - 4/30/2001	19 days	Sp	*Topping et al.* [2004] *(S73)*	NER/A/S/2000/00442, NER/S/A/2000/03653 JDA, NER/S/A/2001/06423 DT and NERC GR3/12499
Storm Peak, CO, USA	INSPECT-2	Rural / Remote	-106.70	40.45	4/4/2004 - 5/2/2004	28 days	Sp	*Richardson et al.* [2007] *(S74)*	NSF ATM-0334308 & ATM-0513116
Duke Forest, NC, USA		Rural / Remote	-79.10	35.97	9/13/2004 - 9/21/2004	7 days	F		EPA RD-83145401
Thompson Farm, NH, USA		Rural / Remote	-70.95	43.11	7/9/2005 - 8/15/2005	38 days	Su	*Cottrell et al.* [2008] *(S75)*	NOAA NA03OAR4600122 and NA04OAR4600154, NSF ATM-0327643, EPA 83216101-0
Pinnacle State Park, NY, USA		Rural / Remote	-76.00	43.00	7/14/2004 - 8/5/2004	22 days	Su	*Bae et al.* [2007] *(S76)*	NYS DEC C004210, NYSERDA 4918ERTERE-S99
Chebogue Pt., Nova Scotia, Canada	ICARTT	Rural / Remote	-66.10	43.76	7/7/2004 - 8/14/2004	38 days	Su	*Williams et al.* [2007] *(S77)*	ICARTT, NOAA NA05OAR4310025, NSF ATM-0449815
Jungfraujoch, Switzerland	CLACE	Rural / Remote	7.60	46.30	6/28/2002 - 7/17/2002	19 days	Su		
Hyytiälä, southern Finland	BACCI & QUEST	Rural / Remote	24.28	61.84	3/31/2005 - 4/15/2005	15 days	Sp	*Raatikainen et al.* [2009] *(S78)*	Maj and Tor Nessling Foundation (grants 2007083 and 2008095), FCoE program (project number 1118615), FiDiPro program, and BACCI and QUEST projects

Table S4: Locations and average concentrations of non-refractory submicron species for the studies in the map of Figure 1. In all cases the averages are over all the available data for each campaign.

Dataset Location	Average Concentration (μg m^{-3}) in submicron aerosols under ambient conditions									
	Sulfate	Nitrate	Ammonium	Chloride	HOA	LV-OOA	SV-OOA	Total OOA	Other OA	Total
Beijing, China	20.3	17.3	13.1	1.10	11.5	12.3	4.3	n/a	n/a	79.9
Tokyo, Japan (Summer)	3.2	1.5	1.9	0.15	1.9	3.2	1.5	n/a	n/a	13.2
Tokyo, Japan (Winter)	1.8	3.9	2.7	0.78	3.7	n/a	n/a	2.3	1.0	16.2
Pittsburgh, PA, USA	7.0	0.9	2.4	0.06	1.4	2.6	0.5	n/a	n/a	14.7
Mexico City, Mexico	3.6	3.5	2.0	0.40	5.0	n/a	n/a	8.1	4.2	26.8
Riverside, CA, USA	3.3	4.3	2.4	0.09	1.2	2.8	4.2	n/a	0.6	19.1
Houston, TX, USA	4.9	0.4	1.5	0.02	0.7	n/a	n/a	2.7	2.6	12.8
Boulder, CO, USA	0.6	0.5	0.3	0.01	0.5	1.0	1.5	n/a	n/a	4.4
New York City, USA (Summer)	3.9	0.7	1.7	0.03	1.1	3.0	1.8	n/a	n/a	12.2
New York City, USA (Winter)	2.4	2.6	1.7	0.18	2.2	n/a	n/a	2.6	n/a	11.6
Vancouver, Canada	0.9	0.6	0.7	0.04	2.4	n/a	n/a	2.5	n/a	7.0
Edinburgh, UK	0.5	0.3	0.3	0.00	0.7	n/a	n/a	1.2	n/a	3.0
Manchester, UK (Summer)	3.4	3.7	2.3	0.00	1.9	n/a	n/a	3.0	n/a	14.3
Manchester, UK (Winter)	0.8	0.8	0.6	0.00	1.0	n/a	n/a	0.6	1.5	5.2
Mainz, Germany	1.2	0.6	0.5	0.04	0.8	n/a	n/a	1.1	n/a	4.3
Zurich, Switzerland (Summer)	1.4	0.8	0.8	0.03	0.5	2.9	1.4	n/a	1.8	9.6
Zurich, Switzerland (Winter)	4.2	8.0	3.9	0.16	0.7	n/a	n/a	5.1	3.5	25.5
Off New England Coast	2.0	0.3	0.7	0.01	0.5	2.1	2.8	n/a	n/a	8.5
Chelmsford, UK	1.7	0.5	0.7	0.04	0.8	1.4	0.4	n/a	n/a	5.3
Taunus, Germany	3.9	1.4	1.4	0.03	1.6	4.5	3.4	n/a	n/a	16.3
Fukue, Japan	4.7	0.5	1.7	0.07	0.5	2.0	1.6	n/a	n/a	11.0
Okinawa, Japan	4.7	0.2	1.3	0.04	n/a	1.2	0.5	n/a	n/a	7.9
Cheju, Korea	3.9	0.8	1.7	0.00	0.3	n/a	n/a	4.0	n/a	10.7
Storm Peak, CO, USA	0.6	0.2	0.4	0.00	0.2	n/a	n/a	0.7	n/a	2.1
Duke Forest, NC, USA	1.1	0.1	0.3	0.00	0.1	0.8	0.5	n/a	n/a	2.8
Thompson Farm, NH, USA	3.0	0.3	0.9	0.01	1.1	1.3	2.9	n/a	n/a	9.5
Pinnacle Park, NY, USA	4.9	0.4	1.3	0.01	0.3	2.7	2.7	n/a	n/a	12.3
Chebogue Pt., Canada	0.9	0.1	0.3	0.00	0.2	0.9	0.6	n/a	n/a	2.9
Jungfraujoch, Switzerland	0.5	0.2	0.3	0.00	n/a	0.8	0.4	n/a	n/a	2.2
Hyytiälä, Finland	0.3	0.3	0.2	0.00	n/a	0.6	0.6	n/a	n/a	2.0

SOM References

S1. J.D. Smith *et al.*, *Atmos. Chem. Phys.* **9**, 3209 (2009).
S2. J.H. Kroll *et al.*, *Phys. Chem. Chem. Phys.* **11**, 8005 (2009).
S3. P.F. DeCarlo *et al.*, *Anal. Chem.* **78**, 8281 (2006).
S4. E.A. Weitkamp, A.M. Sage, J.R. Pierce, N.M. Donahue, and A.L. Robinson, *Environ. Sci. Technol*. **41**, 6969 (2007).
S5. A.M. Sage, E.A. Weitkamp, A.L. Robinson, and N.M. Donahue, *Atmos. Chem. Phys.* **8***,* 1139 (2008).
S6. A.P. Grieshop, J.M. Logue, N.M. Donahue, and A.L. Robinson*, Atmos. Chem. Phys.* **9**, 1263 (2009).
S7. A.P. Grieshop, N.M. Donahue, and A.L. Robinson, *Atmos. Chem. Phys.* **9**, 2227 (2009).
S8. J.T. Jayne *et al.*, *Aerosol Sci. Technol.* **33**, 49 (2000).
S9. M.R. Canagaratna *et al.*, *Mass Spec. Rev.* **26**, 185 (2007).
S10. D. Paulsen *et al*., *Environ. Sci. Technol.* **39**, 2668 (2005).
S11. J. Duplissy *et al.*, *Geophys. Res. Lett.* **35**, L03818 (2008).
S12. M.D. Petters and S.M. Kreidenweis, *Atmos. Chem. Phys.* **7**, 1961 (2007).
S13. A.C. Aiken *et al.*, *Environ. Sci. Technol.* **42**, 4478 (2008).
S14. M.C. Coen *et al.*, *J. Geophys. Res.* **112**, D13213 (2007).
S15. S. Sjogren *et al., Atmos. Chem. Phys.* **8**, 5715 (2008).
S16. R.H. Stokes and R.A. Robinson, *J. Phys. Chem.* **70**, 2126 (1966).
S17. P.F. DeCarlo *et al.*, *Atmos. Chem. Phys.* **8**, 4027 (2008).
S18. R. Gasparini, R.J. Li, and D.R. Collins, *Atmos. Environ.* **38**, 3285 (2004).
S19. M. Ehn *et al.*, *Atmos. Chem. Phys.* **7**, 211 (2007).
S20. J. Joutsensaari, P. Vaattovaara, M. Vesterinen, K. Hameri, and A. Laaksonen*, Atmos. Chem. Phys.* **1**, 51 (2001).
S21. P. Vaattovaara, M. Räsänen, T. Kühn, J. Joutsensaari, and A. Laaksonen. *Atmos. Chem. Phys.* 5, 3277 (2005).
S22. P. Tiitta *et al., Atmos. Environ.,* doi:10.1016/j.atmosenv.2009.06.021, *in press* (2009).
S23. J. Duplissy *et al.*, *Atmos. Meas. Tech.,* **2**, *363 (*2009).
S24. P. Paatero, *Chemom. Intell. Lab. Syst.* **37** 23 (1997).
S25. V.A. Lanz *et al., Atmos. Chem. Phys.* **7**, 1503 (2007).
S26. I.M. Ulbrich, M.R. Canagaratna, Q. Zhang, D.R. Worsnop, and J.L. Jimenez, *Atmos. Chem. Phys.* **9**, 2891 (2009).
S27. J.F. Pankow*, Atmos. Environ.* **28**, 189 (1994).
S28. J.R. Odum, T.P.W. Jungkamp, R.J. Griffin, R.C. Flagan, and J.H. Seinfeld*, Science* **276**, 96 (1997).
S29. M.K. Shrivastava, E.M. Lipsky, C.O. Stanier, A.L. Robinson, *Environ. Sci. Technol.* **40**, 2671 (2006).
S30. J.A. Huffman *et al., Environ. Sci. Technol.* **43**, 5351 (2009).
S31. J.A. Huffman *et al., Atmos. Chem. Phys.* **9**, 7161 (2009).
S32. N.M. Donahue, A.L. Robinson, C.O. Stanier, and S.N. Pandis, *Environ. Sci. Technol.* **40**, 2635 (2006).
S33. N.M. Donahue, A.L. Robinson, and S.N. Pandis, *Atmos. Environ.* **43,** 94 (2009).

S34. K. Dzepina *et al.*, *Atmos. Chem. Phys.* **9**, 5681 (2009).
S35. L. Vereecken and J. Peeters. *Phys. Chem. Chem. Phys.* **4**, 467 (2002).
S36. A.T. Lambe, J.Y. Zhang, A.M. Sage, and N.M. Donahue*, Environ. Sci. Technol.* **41**, 2357 (2007).
S37. J.F. Pankow and W.E. Asher, *Atmos. Chem. Phys.* **8**, 2773 (2008).
S38. J.F. Pankow and K.C. Barsanti, *Atmos. Environ.* **43**, 2829 (2009).
S39. D.M. Murphy, D.J. Cziczo, P.K. Hudson, D.S. Thomson, *J. Geophys. Res.* **112**, D04203 (2007).
S40. I.J. George, J. Slowik, and J.P.D. Abbatt*, Geophys. Res. Lett.,* **35**, L13811 (2008).
S41. J.E. Shilling *et al.*, *Atmos. Chem. Phys.* **9,** 771 (2009).
S42. A.P. Grieshop, N.M. Donahue, and A.L. Robinson, *Geophys. Res. Lett.* **34**, L14810 (2007).
S43. K.S. Docherty *et al.*, *Environ. Sci. Technol.* **42**, 7655 (2008).
S44. J. Sun *et al.*, *Atmos. Environ.* doi:10.1016/j.atmosenv.2009.03.020, in press (2009).
S45. N. Takegawa *et al.*, *Aerosol Sci. Technol.* **39**, 760 (2005).
S46. N. Takegawa *et al.*, *J. Geophys. Res.* **111**, D11206 (2006).
S47. Q. Zhang *et al.*, *Environ. Sci. Technol.* **38**, 4797 (2004).
S48. Q. Zhang, M.R. Canagaratna, J.T. Jayne, D.R. Worsnop, and J.L. Jimenez, *J. Geophys. Res.* **110**, D07S09 (2005).
S49. Q. Zhang *et al.*, *Environ. Sci. Technol.* **39**, 4938 (2005).
S50. Q. Zhang, D.R. Worsnop, M.R. Canagaratna, and J.L. Jimenez, *Atmos. Chem. Phys.* **5**, 3289 (2005).
S51. Q. Zhang, J.L. Jimenez, D.R. Worsnop, and M.R. Canagaratna, *Environ. Sci. Technol.* **41**,3213 (2007).
S52. A.C. Aiken *et al.*, *Atmos. Chem. Phys.* **9**, 6633 (2009).
S53. M.J. Cubison *et al.*, *Atmos. Chem. Phys.* **6**, 5573 (2008).
S54. P. Tanaka *et al.*, *Atmos. Environ.* **37**, 1393 (2003).
S55. E. Nemitz *et al.*, *Aerosol Sci. Technol.* **42**, 636 (2008).
S56. F. Drewnick *et al.*, *Aerosol Sci. Technol.* **38**, 92 (2004a).
S57. F. Drewnick *et al.*, *Aerosol Sci. Technol.* **38**, 104 (2004b).
S58. S. Weimer *et al.*, *J. Geophys. Res.* **111**, D18305 (2006).
S59. H. Boudries *et al.*, *Atmos. Environ.* **38**, 5759 (2004).
S60. M.R. Alfarra *et al.*, *Atmos. Environ.* **38**, 5745 (2004).
S61. J.D. Allan *et al.*, *J. Geophys. Res.* **108**, 4090 (2003a).
S62. J.D. Allan *et al.*, *J. Geophys. Res.* **108**, 4091 (2003b).
S63. B.P. Vester *et al.*, *Atmos. Environ.* **41**, 6102 (2007).
S64. V. Lanz *et al.*, *Environ. Sci. Technol.* **42**, 214 (2008).
S65. J. de Gouw *et al.*, *J. Geophys. Res.* **110**, D16305 (2005).
S66. C. Marcolli *et al.*, *Atmos. Chem. Phys.* **6**, 5649 (2006).
S67. T.S. Bates, P.K. Quinn, D.J. Coffman, J.E. Johnson, and A.M. Middlebrook, *J. Geophys. Res.* **110**, D18202 (2005).
S68. M.J. Cubison *et al.*, *Atmos. Chem. Phys.* **6**, 5573 (2006).
S69. U. Dusek *et al. Science* **312**, 1375 (2006).
S70. S. Hings, S. Walter, J. Schneider, S. Borrmann, and F. Drewnick, *Aerosol Sci. Technol.* **41**, 679 (2007).
S71. A. Takami, T. Miyoshi, A. Shimono, S. Hatakeyama, *Atmos. Environ.* **20**, 4913

(2005).
S72. T. Miyoshi *et al.*, *J. Geophys. Res.*, submitted (2009).
S73. D. Topping *et al.*, *Atmos. Environ.*, **38**, 2111 (2004).
S74. M.S. Richardson *et al.*, *J. Geophys. Res.* **112**, D02209 (2007).
S75. L. Cottrell *et al.*, *J. Geophys. Res.* **113**, D08212 (2008).
S76. M.S. Bae, K.L. Demerjian, and J.J. Schwab, *Atmos. Environ.* **39**, 7467 (2006).
S77. B.J. Williams *et al.*, *J. Geophys. Res.* **112**, D10S26 (2007).
S78. T. Raatikainen *et al.*, *Atmos. Chem. Phys. Discuss.* **9**, 21847 (2009).

ATMOSPHERIC SCIENCE

A New Look at Aging Aerosols

As organic aerosols from different sources age in the atmosphere, their properties become remarkably similar.

Meinrat O. Andreae

To chemists, studying the composition of the organic matter in atmospheric aerosols has been frustrating. Despite years of effort and the use of the most sophisticated techniques available, only ~10 to 30% of the particulate organic matter (POM) has been identified as specific compounds (*1*). Given that POM makes up a major part of the atmospheric aerosol, this implies that typically the composition of about half of the material in atmospheric aerosols cannot be characterized as individual compounds. On page 1525 of this issue, Jimenez *et al*. (*2*) show that the effects of organic aerosol on atmospheric chemistry and climate can be discerned without knowing every one of its components. They propose a new conceptual framework that reflects the emerging view of organic aerosol as a dynamic component of atmospheric chemistry.

Spectroscopic studies have shown that POM contains numerous types of organic molecules, including hydrocarbons, alcohols, aldehydes, and carboxylic acids (*3*, *4*). The unidentified compounds in POM are thought to be a highly complex mixture of combinations of these molecular structures, resulting from oxidation, condensation, and oligomerization of atmospheric hydrocarbons. Conventional analytical techniques require large samples and sampling times of up to a week, and thus the prevailing view of organic aerosols has been that they are a static mixture of ill-defined "organic matter." Because of the limited information available, organic aerosol was thought to have an uneventful life in the atmosphere, beginning with emission from tailpipes or production from oxidation of organic gases, and ending by deposition as dust or in rain.

The transformational event in this story was the invention and widespread use of the aerosol mass spectrometer (*5*). With this instrument, aerosols in the size range of ~50 to 1000 nm can be analyzed with a time resolution of 1 min, providing chemical information about inorganic species and organic molecular structural components. This tool has vastly increased the information available on the organic component of the atmospheric aerosol (*2*, *6*, *7*) and made it possible to relate changes in the composition, size, and amount of the organic components to chemical and physical processes in the atmosphere.

Identification of individual organic species remains an unattainable, but probably not so important, goal. Instead, the aerosol mass spectrometer provides information about chemical properties such as the ratio of oxygen to carbon, the relative abundance of hydrocarbon-like structures, and a variety of molecular fragments. This information allows POM to be classified into a small number of categories that relate to their oxidation state and volatility. This, in turn, provides clues about the origin and processing history of the organic aerosol.

A key concept to emerge is that the organic aerosol is a continuum in a complex space of variables, such as chemical reactivity, degree of oxidation, molecular weight, light absorption, and hygroscopicity (the ability to take up water as the ambient relative humidity rises). Volatility, for example, spans from gaseous compounds, such as isoprene, to humic acid–like substances that resist heating to several hundred degrees (*8*). Light absorption ability ranges from completely colorless substances to utterly black organic matter (*9*). These variables are crucial for the ways in which organic matter behaves in the atmosphere and how it affects climate.

Volatility regulates whether a compound is present as a vapor or as condensed matter. This in turn determines whether a substance is more likely to be subject to chemical transformations by gas- or condensed-phase reactions. A large fraction of the atmospheric organic matter is semivolatile and thus readily exchanges between gas and aerosol, allowing a highly dynamic sequence of processes. For example, a compound may move into the gas phase, where it is subject to oxidation reactions by ozone or the hydroxyl radical (OH), followed by recondensation of the less volatile oxidation product, and so on (*10*). These reaction chains may begin with a molecule of intermediate molecular weight, such as a terpene, which may then undergo oxidation or oligomerization reactions leading to larger molecules, or fragmentation reactions that produce smaller molecules, with CO_2 as the end product. Given the wide variety of starting compounds (both natural and of human origin) that are emitted into the atmosphere, and the complex reaction paths possible in the gas and condensed phases, a myriad of compounds can be formed, with little hope of ever identifying each individually.

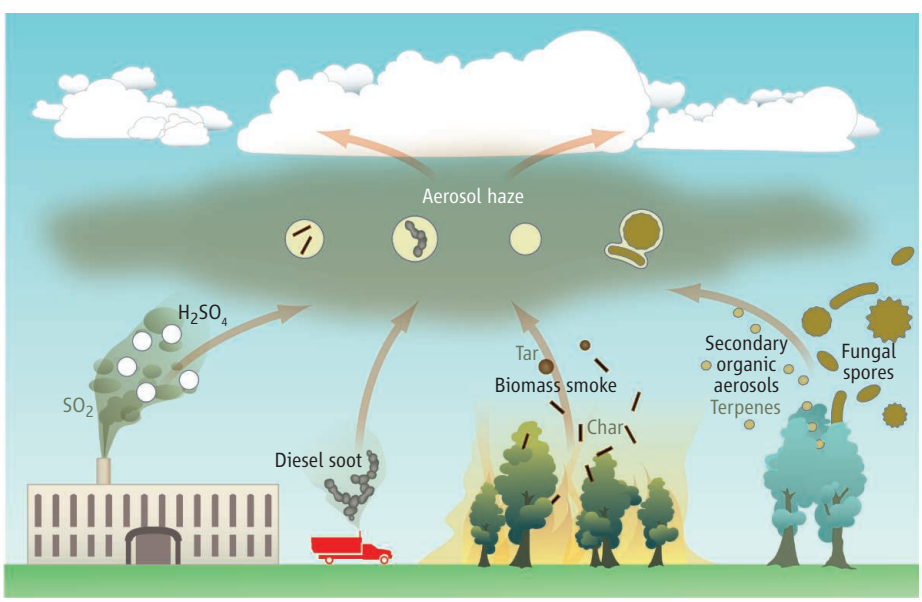

Effects of aging. Organic aerosols from different sources undergo chemical processing and mix with each other as well as with inorganic aerosols. This leads to a convergence in their chemical and optical properties and in their ability to nucleate cloud droplets.

Max Planck Institute for Chemistry, 55020 Mainz, Germany. E-mail: m.andreae@mpic.de

Published by AAAS

Fortunately, such identification may not be necessary, or even particularly helpful, for understanding the role of organic aerosols in atmospheric chemistry and climate, because some of the key variables mentioned above are interrelated and can be derived from properties that can be measured relatively easily. Hygroscopicity is an interesting example: It determines how readily a particle can take up water in a nascent cloud and thus nucleate a cloud droplet, an important way in which aerosols influence climate (*11*). Jimenez *et al*. show that the hygroscopicity of POM increases in close correlation with its degree of oxidation as measured by aerosol mass spectrometry, indicating that the cloud-nucleating ability of organic aerosols increases as a result of atmospheric chemical processing. Similarly, light absorption by POM increases during aging as a result of the formation of "brown carbon" (*12*), which affects climate and atmospheric chemistry by absorbing solar radiation.

A remarkable consequence of the atmospheric evolution of POM is the convergence of chemical and physical properties in aerosols of very diverse origin as they age (see the figure). Organic matter produced from pollutants in urban atmospheres, from biogenic emissions in forests, or from terpenes exposed to photochemical reactions in smog chambers all progress to POM of similar oxidation state, hygroscopicity, volatility, and molecular mass. The dynamic exchange of semivolatile substances facilitates the exchange of organic molecules between particles of different origin, promoting, for example, the coating of soot carbon particles with soluble organic matter.

These observations render almost obsolete the classical distinction between primary and secondary atmospheric particles—that is, those emitted as particles and those formed in the atmosphere. They also help to explain the striking similarity in the cloud-nucleating ability of particles from such diverse locations as Mexico City and the remote Amazon rainforest (*13*, *14*). This convergence is a great advantage to climate modelers, because it reduces the amount of complexity that must be represented in models that investigate aerosol effects on climate.

References

1. B. R. T. Simoneit *et al*., *J. Geophys. Res.* **109**, D19S10 (2004).
2. J. L. Jimenez *et al*., *Science* **326**, 1525 (2009).
3. S. Fuzzi *et al*., *Geophys. Res. Lett.* **28**, 4079 (2001).
4. S. Takahama, S. Gilardoni, L. M. Russell, A. L. D. Kilcoyne, *Atmos. Environ.* **41**, 9435 (2007).
5. M. R. Canagaratna *et al*., *Mass Spectrom. Rev.* **26**, 185 (2007).
6. S. R. Zorn, F. Drewnick, M. Schott, T. Hoffmann, S. Borrmann, *Atmos. Chem. Phys.* **8**, 4711 (2008).
7. Q. Zhang *et al*., *Geophys. Res. Lett.* **34**, L13801 (2007).
8. A. L. Robinson *et al*., *Science* **315**, 1259 (2007).
9. M. O. Andreae, A. Gelencsér, *Atmos. Chem. Phys.* **6**, 3131 (2006).
10. N. M. Donahue, A. L. Robinson, C. O. Stanier, S. N. Pandis, *Environ. Sci. Technol.* **40**, 2635 (2006).
11. M. O. Andreae, D. Rosenfeld, *Earth Sci. Rev.* **89**, 13 (2008).
12. A. Gelencsér *et al*., *J. Atmos. Chem.* **45**, 25 (2003).
13. Y. Shinozuka *et al*., *Atmos. Chem. Phys.* **9**, 6727 (2009).
14. S. S. Gunthe *et al*., *Atmos. Chem. Phys.* **9**, 7551 (2009).

10.1126/science.1183158

MEDICINE

A Reinnervating MicroRNA

Robert H. Brown

A microRNA expressed in skeletal muscle promotes the regeneration of neuromuscular synapses after injury and in a neurodegenerative disease model.

MicroRNAs are small noncoding RNAs (~22 nucleotides in length) that negatively regulate gene expression at the posttranscriptional level by binding to the 3′-untranslated region of target RNAs. Over the past 15 years, critical roles for microRNA have been established in regulating cell proliferation, differentiation and development, and death (*1*). Recent investigations have implicated microRNA networks in diverse disorders, such as cancer and cardiac disease. On page 1549 in this issue, Williams *et al*. (*2*) define a role for a microRNA (miR-206) in reinnervating the neuromuscular junction after injury and improving survival in a mouse model of the neurodegenerative disease amyotrophic lateral sclerosis (ALS). The findings provide insight into the molecular basis of neuromuscular junction plasticity in the adult and also into determinants of rates of disease progression in motor neuron disease.

Motivated by the observation that microRNAs mediate stress responses in muscle, Williams *et al*. sought evidence that microRNAs are dysregulated in the muscle of a transgenic line of the ALS mouse model. In these transgenic ALS mice, a mutant form of the enzyme superoxide dismutase protein (SOD1) was expressed, which triggers adult-onset motor neuron death. In normal mice, sciatic nerve injury, which results in denervation of muscle, increases expression of miR-206 in the muscle. When miR-206 was inactivated in ALS mice, the time from disease onset to death was shortened, indicating that miR-206 is protective in ALS. Similarly, inactivation of miR-206 in normal adult mice adversely influenced the response of the neuromuscular junction to nerve injury. In the absence of miR-206, axonal regrowth toward the denervated neuromuscular junction was normal, but innervation of the junctional endplates (the muscle fiber membrane at the junction between muscles and nerves) was delayed. Moreover, the neuromuscular junctions that did form were morphologically defective. Remarkably, loss of miR-206 had no impact on the normal development of the neuromuscular junctions in uninjured embryos and young mice, indicating a relatively specific role for mir206 in junction maintenance and regeneration in the adult.

Neurology, Biochemistry and Molecular Pharmacology and Program in Neuroscience, University of Massachusetts Medical School, 55 Lake Avenue North, Worcester, MA 01655, USA. E-mail: robert.brown@umassmed.edu

Williams *et al*. further documented that miR-206 represses the expression of of histone deacetylase 4 (HDAC4) in muscle cells. HDAC4 normally inhibits nerve reinnervation by blocking expression of fibroblast growth factor binding protein 1 (FGFBP1). FGFBP1 is thought to potentiate the actions of FGF proteins (FGF7, 10, and 22) on distal motor neuron terminals and thereby promote innervation. Thus, there is a reciprocal interaction between miR-206 and HDAC4; the former facilitates and the latter inhibits reinnervation (see the figure).

These findings are of considerable interest from several perspectives. It is evident that the miR-206–HDAC4–FGFBP1 signaling pathway is important in maintaining the integrity and plasticity of the adult neuromuscular junction. The importance of microRNA function during normal development of the brain is well established. In the nervous system, for example, inactivation of mechanisms that generate microRNA severely disrupts brain structure (*3*, *4*). Less well defined is a role for microRNA in maintaining homeostasis at the neuromuscular junction in the mature nervous system. Williams *et al*. convincingly show that, although it is not essential for normal